



TALLINN UNIVERSITY OF TECHNOLOGY

SCHOOL OF ENGINEERING

Department of Electrical Power Engineering and Mechatronics

DESIGN OF A MAINS-POWERED INDOOR AIR QUALITY MONITOR WITH RADIO INTERFACE

VÕRGUTOITEL RAADIOLIIDSEGA SISEÕHUKVALITEEDI MÕÕTESEADME VÄLJATÖÖTAMINE

MASTER THESIS

Student: Kevin Lüüde
Student code: 212049MAHM
Supervisor: Martin Jaanus, Senior Lecturer
Co-supervisor: Kalle Arulaane, Conversion Electronics,
Owner

Tallinn, 2024

AUTHOR'S DECLARATION

Hereby I declare, that I have written this thesis independently.

No academic degree has been applied for based on this material. All works, major viewpoints and data of the other authors used in this thesis have been referenced.

"....." 202.....

Author:
/signature /

Thesis is in accordance with terms and requirements

"....." 202....

Supervisor:
/signature/

Accepted for defence

".....".....202... .

Chairman of theses defence commission:
/name and signature/

Non-exclusive Licence for Publication and Reproduction of Graduation Thesis¹

I, Kevin Lüüde hereby

1. grant Tallinn University of Technology (TalTech) a non-exclusive license for my thesis

“Design of a mains-powered indoor air quality monitor with radio interface”,

supervised by Martin Jaanus and co-supervised by Kalle Arulaane,

- 1.1 to be reproduced for the purposes of preservation and electronic publication of the graduation thesis, incl. to be entered in the digital collection of TalTech library until expiry of the term of copyright;
 - 1.2 to be published via the web of TalTech, incl. to be entered in the digital collection of TalTech library until expiry of the term of copyright.
2. I am aware that the author also retains the rights specified in clause 1 of this license.
3. I confirm that granting the non-exclusive license does not infringe third persons' intellectual property rights, the rights arising from the Personal Data Protection Act or rights arising from other legislation.

_____ (date)

¹ The non-exclusive licence is not valid during the validity of access restriction indicated in the student's application for restriction on access to the graduation thesis that has been signed by the school's dean, except in case of the university's right to reproduce the thesis for preservation purposes only. If a graduation thesis is based on the joint creative activity of two or more persons and the co-author(s) has/have not granted, by the set deadline, the student defending his/her graduation thesis consent to reproduce and publish the graduation thesis in compliance with clauses 1.1 and 1.2 of the non-exclusive licence, the non-exclusive license shall not be valid for the period.

ABSTRACT

Author: Kevin Lüüde

Type of the work: Master Thesis

Title: Design of a mains-powered indoor air quality monitor with radio interface

Date: 13.05.2024

81 pages (the number of thesis pages including appendices)

University: Tallinn University of Technology

School: School of Engineering

Department: Department of Electrical Power Engineering and Mechatronics

Supervisor(s) of the thesis: Senior Lecturer Martin Jaanus, Kalle Arulaane

Consultant(s):

Abstract:

The aim of this thesis is to develop an integral part of a novel mains-powered indoor air quality monitor with radio interface. This device comprises two main parts: an offline power supply and a sensor board. The sensor board contains various air quality sensors, as well as a radio module with an antenna for wireless communications. The power supply is designed in isolated flyback topology to supply the sensor board with DC voltage. The power supply and sensor board are connected and assembled to a frame which enables its installation inside a common junction box.

In this thesis, several existing indoor air quality monitoring solutions are first examined as reference for the currently developed device. Next, physical design constraints are established since the device is installed inside a junction box with limited space. The antenna selection, design of the antenna circuit and its performance verification on the finalized radio module are further covered in detail. Lastly, a prototype of the power supply is designed.

As a result of this thesis, the design of the flyback power supply prototype and the sensor board including its radio module will be finalized and tested. The results of these tests provide information whether the developed system components are adequate for the current application or if further improvements need to be made.

Keywords: indoor air quality, air quality monitors, isolated flyback power supply, chip antenna, air quality sensors

LÕPUTÖÖ LÜHIKOKKUVÕTE

Autor: Kevin Lüüde

Lõputöö liik: Magistritöö

Töö pealkiri: Võrgutoitel raadioliidesega siseõhukvaliteedi mõõteseadme väljatöötlus

Kuupäev: 13.05.2024

81 lk (lõputöö lehekülgede arv koos lisadega)

Ülikool: Tallinna Tehnikaülikool

Teaduskond: Inseneriteaduskond

Instituut: Elektroenergeetika ja mehhatroonika instituut

Töö juhendaja(d): Vanemlektor Martin Jaanus, Kalle Arulaane

Töö konsultant (konsultandid):

Sisu kirjeldus:

Käesoleva töö eesmärgiks on välja töötada oluline osa uudest siseõhukvaliteedi monitorist, mis töötab võrgutoitel ning võimaldab juhtmevaba suhtlust kasutades selleks raadioliidest. Seadme arendamisele kuuluva osa kaks peamist üksust on selle toitelahendus ja andurplaat. Viimane hõlmab lisaks erinevatele õhukvaliteedi anduritele ka antenniga raadiomoodulit juhtmevabaks suhtluseks kasutajaga. Andurplaadi varustamiseks alalispingega on disainitud toiteplokk isoleeritud „flyback” topoloogias. Toitelahendus ja andurplaat on omavahel ühendatud ning paigaldatud spetsiaalse raami sisse, mis võimaldab nende kinnitamist harukarpi.

Antud töös on esmalt vaadeldud erinevaid olemasolevaid siseõhukvaliteeti jälgivaid lahendusi, et tekiks võrdluspunkt nende ja antud töös arendatava seadme põhiparameetrite vahel. Järgmiseks on seadmele seatud füüsilised piirangud, mis tulenevad harukarbi piiratud mõõtmetest. Töös on kajastatud ka seadme erinevate osade arendust, täpsemalt seda, mis hõlmab antenni valikut ja selle testimist valmis raadiomoodulil ning samuti ka „flyback” toitemuunduri disainiprotsessi.

Lõputöö tulemusena valmivad toiteploki prototüüp ning andurplaat koos raadiomooduliga. Nende testimisel saadud tulemuste põhjal on võimalik järeldada, kas väljatöötatud seadme osad täidavad seatud eesmäärke või on vaja teatud osade arendustööga jätkata.

Märksõnad: siseõhukvaliteet, siseõhukvaliteedimonitor, isoleeritud „flyback” toiteplokk, antenn, õhukvaliteediandurid

THESIS TASK

Student: Kevin Lüüde, 212049MAHM
Study programme MAHM02/18 - Mechatronics
Main speciality: Mechatronics
Supervisor(s): Martin Jaanus, Senior Lecturer, 6203802
Kalle Arulaane, Conversion Electronics OÜ, Owner

Consultant:

Thesis topic:

DESIGN OF A MAINS-POWERED INDOOR AIR QUALITY MONITOR WITH RADIO INTERFACE

VÕRGUTOITEL RAADIOLIIDSEGA SISEÕHUKVALITEEDI MÕÕTESEADME
VÄLJATÖÖTLUS

Thesis main objectives:

1. Establishing design constraints on the indoor air quality monitoring device
2. Selection of a viable chip antenna and design of the antenna circuit
3. Design of a power supply prototype in isolated flyback topology

Thesis tasks and time schedule:

No	Task description	Deadline
1.	Establishing physical design constraints	01.2023
2.	Power supply topology research	01.2023
3.	Preliminary chip antenna selection	02.2023
4.	Preliminary flyback transformer and controller selection	04.2023
5.	Finalize the design of antenna test boards	04.2023
6.	Complete antenna board testing	06.2023
7.	Power converter evaluation board testing	07.2023
8.	Final flyback transformer and controller selection	09.2023
9.	Power supply prototype design	10.2023

10.	Power supply prototype testing	11.2023
11.	Comparative tests with the finalized radio module	11.2023
12.	Literature review on existing air quality monitoring solutions	04.2024
13.	Finalize writing of thesis	10.05.2024
14.	Submission of thesis	13.05.2024

Language: english

Deadline for submission of thesis:

".....".....20.....a

Student: ".....".....20.....a

/signature/

Supervisor: ".....".....20.....a

/signature/

Head of study programme:

..... ".....".....20.....a

/signature/

CONTENTS

ABSTRACT	4
LÕPUTÖÖ LÜHIKOKKUVÕTE	5
THESIS TASK	6
PREFACE	10
LIST OF ABBREVIATIONS AND SYMBOLS	11
1 INTRODUCTION.....	12
2 LITERATURE REVIEW AND BACKGROUND	14
2.1 Existing indoor air quality monitoring solutions	14
2.1.1 Comparison of the IAQ monitoring solutions	17
2.2 Antenna basics	19
2.2.1 Impedance consideration	19
2.2.2 Antenna parameters	22
2.2.3 Impedance matching	24
2.3 Power supply topology selection	26
2.4 Flyback Topology	27
3 DEVELOPMENT OF THE SENSOR BOARD	33
3.1 Physical constraints on the system.....	33
3.2 Design of the antenna circuit.....	36
3.2.1 Design considerations	37
3.2.2 Antenna feed	38
3.3 Antenna testing	41
3.3.1 Network analyzer test results	42
3.3.2 Radio module test results	44
4 DESIGN OF THE POWER SUPPLY.....	48
4.1 Safety Considerations.....	49
4.2 Flyback transformer and controller selection	52

4.3 Flyback transformer testing.....	55
4.3.1 Operation mode of the flyback converter.....	56
4.4 Thermal considerations.....	57
4.5 Design of a flyback power supply prototype	60
4.6 Power supply prototype testing.....	66
SUMMARY.....	70
KOKKUVÕTE	72
LIST OF REFERENCES	74
Appendix 1 Power supply prototype schematic	81

PREFACE

The topic of this thesis was presented by a customer company offering the opportunity to participate in the development of a mains-powered indoor air quality monitor. The work related to this thesis project was mainly conducted at Conversion Electronics, owned by Kalle Arulaane, the co-supervisor of this thesis. The equipment and basic data necessary to complete the thesis work were provided by both Conversion Electronics, as well as the customer company.

I would like to thank Kalle Arulaane, the co-supervisor of this thesis, who provided very valuable advice and assistance over the duration of the whole thesis project. Furthermore, I want to express gratitude to the customer company for offering the thesis topic, as well to the thesis supervisor Martin Jaanus, whose advice and feedback were greatly appreciated.

LIST OF ABBREVIATIONS AND SYMBOLS

AC – Alternating current

AQI – Air quality index

CPWG – Coplanar wave guide

CTR – Current transfer ratio

DC – Direct current

DCM – Discontinuous conduction mode

DUT – Device under test

EVB – Evaluation board

IAQ – Indoor air quality

IC – Integrated circuit

ICL – Inrush current limiter

IEQ – Indoor environmental quality

IoT – Internet of Things

LDO – Low-dropout regulator

MOSFET – Metal-oxide-semiconductor field-effect transistor

OVC – Overvoltage categories

PCB – printed circuit board

PM_x – Particulate matter with a diameter of up to x μm

PSR – Primary side regulation

RH – Relative humidity

SMPS – Switched mode power supply

SSR – Secondary side regulation

TVOC – Total concentration of volatile organic compounds

VNA – Vector network analyzer

VSWR – Voltage standing wave ratio

WSN – Wireless sensor network

1 INTRODUCTION

To live in a healthy environment, which includes breathing clean air, has been declared a human right by the United Nations General Assembly [1]. This statement is of great significance considering the severity of the potential adverse health effects resulting from poor air quality. Furthermore, adequate indoor air quality is imperative, as most people spend up to 90% of their time indoors [2]. Aside from the social aspect, higher morbidity and mortality rates also place a notable economic burden related to public health costs on the governments worldwide [3]. To improve indoor air quality, it is first important to determine the relevant indoor environmental parameters, define the acceptable ranges for their values, and monitor them. Air quality parameter monitoring is important to determine potential sources of air pollutants, as well as control heating, ventilation, and air conditioning systems intelligently and economically.

The content of the current thesis pertains to the development of integral system components for a novel wireless mains-powered indoor air quality monitoring device for a customer company. Most of the currently available air quality monitoring systems are either battery powered or require an external power supply. However, indoor air quality monitoring devices are generally purposed for long-term use in a typically occupied space requiring adequate indoor air quality. In such cases, battery powered solutions are inconvenient as batteries need to be recharged or changed periodically in order to maintain operation. Devices with external power supplies introduce a different inconvenience, as generally long cables extending from power supplies to devices require additional cable management. Furthermore, visible cables are typically aesthetically unappealing to users. Thus, implementing a mains-powered device that does not require any additional attention nor cable management is advantageous. The current device is designed for installation inside a common junction box analogous to electrical sockets-outlets connected directly to mains. It is therefore installed out of reach of unintended users and unlike most existing devices, its location is fixed for continuity in recorded parameter values.

The first chapter of this thesis examines several existing indoor air quality monitors to provide a comparison with the current solution. The aim of this comparison is to determine if the key features of the current solution are comparable to existing monitors and whether this device can provide improvements in any aspect. Additionally, the basic theoretical aspects of antennas and the flyback converter topology are covered in this

chapter, as this background is necessary to design the antenna circuit and power supply prototype.

The second part of the thesis covers the working principle and development of the different system parts in detail. The first chapter of the second part relates to the design of the sensor board comprising the indoor air quality sensors, as well as the radio module. This includes first establishing the physical constraints on the system, as the device must fit inside a standard junction box. Subsequently, an antenna will be selected based on preliminary testing. After the radio module is finalized, the performance of the selected antenna will also be verified through comparative testing.

The third chapter of the thesis pertains to the design of the first power supply prototype. The most important aspects regarding this part are the relevant safety standards, as the power supply is designed in an isolated topology. Again, size related restrictions must be considered during selection of components. Lastly, tests will be conducted with the power supply prototype to determine whether this design is adequate for use in the current application.

2 LITERATURE REVIEW AND BACKGROUND

This chapter first provides a comprehensive overview and comparison of some of the key features of various existing indoor air quality (IAQ) monitoring devices. Included in the comparison are a selection of indoor air quality monitoring solutions currently available on the market, as well as wireless air quality monitoring designs and proposed solutions covered in various research papers. Furthermore, the basic theoretical aspects necessary to select a suitable antenna and design the antenna circuit are covered. Additionally, different isolated power supply topologies are briefly examined and compared to determine one viable for the current application.

2.1 Existing indoor air quality monitoring solutions

In this section, a selection of wireless indoor air quality monitors currently available on the market are first examined. Key parameters of interest, i.e., the device's source of power, available sensors, and communication technologies, are listed for later comparison with the currently developed solution. It is important to note that the selection of devices includes only those that are suitable for use in Europe. Therefore, a device that is, for instance, specified to work from a 60 Hz 120 V outlet with no alternative options will not be considered. A similar review of various research papers on Internet of Things (IoT) and Wireless Sensor Network (WSN) based IAQ monitoring solutions is then conducted. The purpose of collecting this information is to establish a comparison with the current device to determine whether the features of this solution are adequate for its application and if it can provide an improvement in any aspect. The respective features of the current solution and the devices available on the market are presented in the table below (Table 2.1).

Table 2.1 Comparison of features between the current solution and existing products

Device, [Reference]	Power source	Sensors	Wireless connectivity
Current solution	Device is connected directly to mains inside a junction box	CO ₂ , RH, TVOC, Temperature, AQI based on NO _x and O ₃	ZigBee
uHoo Smart Air Monitor, [4]	External power supply	CO ₂ , CO, O ₃ , NO ₂ , TVOC, PM _{2.5} , RH, Temperature, Air Pressure, Virus Index	Wi-Fi
Qingping Air Monitor [5]	Battery power & external power supply	CO ₂ , TVOC, PM _{2.5} , RH, Temperature	Wi-Fi

Table 2.1 continued

Device, [Reference]	Power source	Sensors	Wireless connectivity
AirGradient ONE [6]	External power supply	CO ₂ , NO _x , TVOC, PM ₁ , PM _{2.5} , PM ₁₀ , RH, Temperature	Wi-Fi, Bluetooth
IKEA Vindstyrka [7]	External power supply	PM _{2.5} , RH, TVOC, Temperature	ZigBee
Airthings View Plus [8]	Battery power & external power supply	CO ₂ , Rn, TVOC, PM _{2.5} , RH, Temperature, Air Pressure	Wi-Fi, Bluetooth
Aranet4 HOME [9]	Battery powered	CO ₂ , RH, Temperature, Air Pressure	Bluetooth
Awair Element [10]	External power supply	CO ₂ , TVOC, PM _{2.5} , RH, Temperature	Wi-Fi, Bluetooth
INKBIRD IAM-T1 [11]	Battery powered	CO ₂ , RH, Temperature, Air Pressure	Bluetooth
Temtop M100 [12]	Battery power & external power supply	CO ₂ , PM _{2.5} , PM ₁₀ , RH, AQI Temperature	Wi-Fi, Bluetooth
Amazon Smart Air Quality Monitor [13]	External power supply	CO, TVOC, PM _{2.5} , RH, Temperature	Wi-Fi, Bluetooth
IQAir AirVisual Pro [14]	Battery power & external power supply	CO ₂ , PM _{2.5} , RH, AQI Temperature	Wi-Fi
Kaiterra Sensedge [15]	Battery power & external power supply	CO ₂ , TVOC, PM _{2.5} , RH, Temperature	Wi-Fi
Atmotube PRO [16]	Battery power & external power supply	TVOC, PM ₁ , PM _{2.5} , PM ₁₀ , RH, Temperature, Air Pressure	Bluetooth

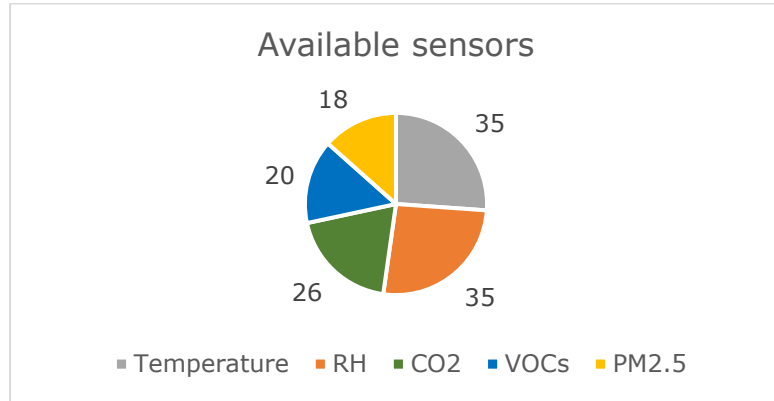
Following the comparison of existing products, review articles [17] and [18] considering various IoT and WSN based IAQ monitoring solutions were referenced to determine studies relevant to the current scope of application. The studies considered were then examined to determine ones that provided sufficient information about the key features of interest required for comparison. For a better overview, the findings are presented in the table below (Table 2.2).

Table 2.2 Comparison of the key features of IAQ monitoring solutions covered in research

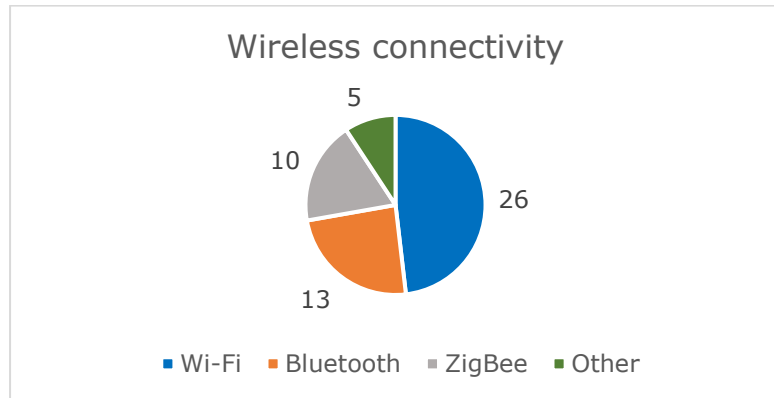
Source of power		
Feature	Reference	No. of studies
External power supply	[19], [20], [21], [22], [23], [24], [25], [26], [27], [28], [29], [30], [31], [32]	14
Battery power (incl. power banks, external and rechargeable batteries)	[24], [28], [30], [31], [33], [34], [35], [36], [37], [38], [39], [40], [41], [42], [43], [44], [45]	17
Solar energy harvesting	[42], [44]	2
Wireless connectivity		
Feature	Reference	No. of studies
Wi-Fi	[20], [21], [22], [24], [25], [26], [27], [28], [29], [30], [32], [33], [35], [38], [39], [40], [41]	17
Bluetooth	[25], [27], [32], [37], [42]	5
ZigBee	[19], [23], [34], [36], [40], [41], [43], [44], [45]	9
LoRa	[24], [26]	2
GPRS	[26]	1
IQRF	[31]	1
GSM	[38]	1
Available sensors		
Feature	Reference	No. of studies
Temperature	[19], [21], [22], [24], [25], [26], [27], [28], [29], [30], [31], [32], [35], [36], [38], [39], [40], [41], [42], [43], [45]	21
Relative humidity (RH)	[19], [21], [22], [24], [25], [26], [27], [28], [29], [30], [31], [32], [35], [36], [38], [39], [40], [41], [42], [43], [45]	21
Carbon dioxide (CO ₂)	[19], [23], [25], [26], [27], [28], [30], [31], [36], [37], [38], [39], [40], [42], [45]	15
Carbon monoxide (CO)	[19], [28], [32], [33], [39], [40], [41]	7
Volatile organic compounds (VOCs)	[22], [24], [26], [32], [33], [34], [35], [36], [39], [42], [44]	11
PM ₁	[20]	1
PM _{2.5}	[20], [21], [24], [26], [35], [36], [41]	7
PM ₁₀	[20], [21], [28], [32], [41]	5
Sulfur dioxide (SO ₂)	[19], [41]	2
Nitrogen dioxide (NO ₂)	[19], [28], [33], [41], [43]	5
Ozone (O ₃)	[19], [41]	2
Chlorine (Cl ₂)	[19]	1
Liquefied petroleum gas	[34], [35]	2
Air quality index (AQI)	[29], [43]	2
Combustible gases	[27], [33], [34], [35]	4

2.1.1 Comparison of the IAQ monitoring solutions

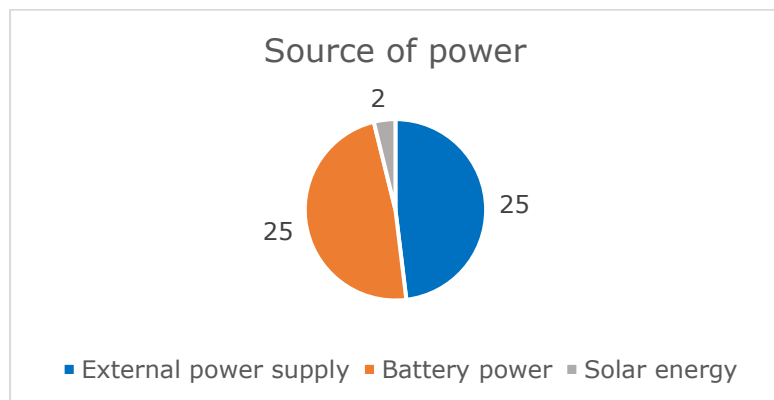
In total, 13 existing products and 27 IAQ monitoring solutions covered in research papers were reviewed for the comparison. The most common features of interest for each of the three considered categories are presented in the charts below (Figure 2.1).



a) The 5 most common types of sensors used in the reviewed IAQ monitors



b) The most common wireless communication technologies used in the IAQ monitors



c) The different sources of power used in the IAQ monitors

Figure 2.1 The most common features used in the reviewed IAQ monitoring solutions
 RH – relative humidity, CO₂ – carbon dioxide, VOCs – volatile organic compounds, PM_{2.5} - particulate matter with diameter less than or equal to 2,5 μm

It was determined that temperature, relative humidity, carbon dioxide, volatile organic compounds, and fine particulate matter with a diameter of up to 2,5 micrometers are the most common qualities to be detected by various IAQ monitors. These parameters were featured in considerably more IAQ monitoring solutions when compared to the rest, as the next most common IAQ parameter was carbon monoxide with just 9 mentions. This suggests that these five parameters are generally considered the most important to provide an adequate indication of the IEQ in a monitored space. As it pertains to the available sensors, the current device features sensing capability for four of the five most common IEQ parameters. Due to the limited board space and relatively large dimensions of PM_{2.5} sensors currently on the market, monitoring of this parameter is not included in the first version of the device. However, a future iteration could also feature a new small-scale PM_{2.5} sensor by Bosch Sensortec [46], which has been announced but not yet released at the time of conducting the literature review.

Of the wireless communication technologies utilized in the reviewed IAQ monitors, all but one device enabled the use of either Wi-Fi, Bluetooth, or ZigBee. This suggests that these communication technologies are both feasible and practical for wireless communications in IAQ monitors. The ZigBee based communication employed in the current solution evidently aligns with the methods found in other reviewed solutions used for similar applications.

It is notable that all reviewed devices are either battery powered or require an external power supply, e.g., an AC-DC adapter. Battery powered solutions, however, are inconvenient as batteries need to be replaced or recharged periodically. This particularly becomes a problem when these devices are installed in difficult to access locations or when numerous battery powered devices are spread around a large area, e.g., in schools, office buildings and hospitals. As IAQ monitors are devices which are generally intended to work unattended in the background, any additional attention they require is undesirable. This problem was considered in designs covered in research papers [42] and [44], which also featured energy harvesting using a solar panel. However, solar energy harvesting is not viable in many indoor applications.

While the use of an external power supply eliminates the inconvenience of batteries, it introduces other issues. With the increasing number of electronic devices in everyday use, requiring additional cable connections for IAQ monitors is not ideal, given that these devices are generally installed in a number of commonly occupied spaces throughout the building. Relatively long cable connections from power outlets to the IAQ monitors

are undesirable from an aesthetic perspective and require additional cable management. The current solution features a power supply within the enclosure of the device itself. It is connected directly to the mains inside a junction box eliminating the need for cable management on the part of the user. The device is mounted flush with the frame of a power outlet to maintain aesthetic appeal. Unlike the IAQ monitors considered in this review this installation also prevents unintended users from accessing this device. Moreover, the current monitor does not require additional attention like battery powered devices and should work practically unattended through its specified lifetime.

2.2 Antenna basics

The antenna is an integral part of the current IAQ monitor, as the device must transmit the sensor data to the user wirelessly. Therefore, some of the basic aspects regarding its operation principle from the perspective of signal transmission are covered. Additionally, the theoretical basis of certain antenna parameters used to determine the viability of an antenna in this application are examined. In general terms, an antenna is a conductor exposed in space with a physical length that is a certain ratio or multiple of the wavelength of the received or transmitted signal. If this condition is met, the antenna is said to be in resonance, as the electrical energy fed from the signal generator to the antenna via antenna feed is radiated into free space in the form of electromagnetic radiation. The antenna feed, or equivalently, the feed line, is the transmission line through which the generated signal travels to the antenna. [47]

2.2.1 Impedance consideration

An antenna has an input impedance that comprises a real and imaginary part which can be represented as follows [48]:

$$Z_{in} = R_{in} + jX_{in} , \quad (2.1)$$

where Z_{in} – input impedance of the antenna, Ω

R_{in} - real part of the antenna input impedance, Ω

X_{in} - imaginary part of the antenna input impedance, Ω .

Furthermore, the feed line of the antenna has an impedance known as the nominal or equivalently, characteristic impedance denoted by Z_0 . If the antenna input impedance is not closely matched to the characteristic impedance, a discontinuity known as an impedance mismatch occurs. This effect is undesirable, as it causes some of the incident power to be reflected at the point of the impedance discontinuity. Therefore, it is often useful to match the antenna input impedance to the characteristic impedance, typically $Z_0 = 50 \Omega$. However, it is important to note that the impedance mismatch between the feed line and antenna is generally a concern only at higher frequencies. At lower frequencies, where the length of the transmission line connecting the transceiver to the antenna is much smaller than the wavelength, i.e., by a factor of ten or more, the transmission line can generally be neglected. At higher frequencies, where the length of the transmission line becomes significant with respect to the wavelength, impedance mismatch between the transmission line and antenna results in notable power loss due to reflections. Depicted below is a general case representing power transfer from a source to a load, e.g., an antenna in this application (Figure 2.2). [47], [48], [49]

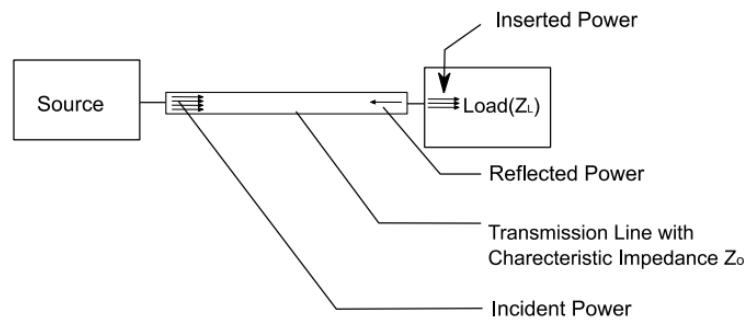


Figure 2.2 General representation of power transfer from a source to a load via a transmission line [47]

The input impedance measured at distance L from the load can be determined with the following equation [47], [49]:

$$Z_{in,L} = Z_0 \cdot \frac{Z_{in} + j \cdot Z_0 \cdot \tan\left(\frac{2\pi}{\lambda} \cdot L\right)}{Z_0 + j \cdot Z_{in} \cdot \tan\left(\frac{2\pi}{\lambda} \cdot L\right)}, \quad (2.2)$$

where $Z_{in,L}$ - input impedance measured at a distance L from the load, Ω ,
 Z_0 - characteristic impedance of the transmission line, Ω ,
 λ - wavelength of the transmitted signal, m,
 L - distance from the load, m.

More generally, equation 2.2 applies for any given point in the transmission line as the parameter L then denotes the distance from the load, e.g., an antenna in the current application [47]. However, from equation 2.2 it is evident that matching the antenna input impedance to the impedance of the transmission line, i.e., $Z_{in} = Z_0$ renders the input impedance $Z_{in, L}$ independent from the length of the transmission line itself. Hence, a circuit where this condition is fulfilled can be considered equivalent to the condition where the length of the transmission line is insignificant with respect to the signal wavelength. To determine the power delivered from the source to the antenna during signal transmission, the impedance of the transceiver must also be considered. The value of the power delivered can be calculated with the following equation [49]:

$$P_{ant} = \frac{V^2 \cdot Z_{in}}{(Z_{in} + Z_s)^2}, \quad (2.3)$$

where P_{ant} - power delivered to the antenna, W,
 V - output voltage from the transceiver, V,
 Z_s - impedance of the transceiver, Ω .

To maximize power transfer, the impedance of the transceiver should also be matched to the antenna feed characteristic impedance or equivalently, the antenna input impedance assuming they are matched. This condition is satisfied if the impedance of the transceiver Z_s is the complex conjugate of the antenna input impedance Z_{in} , i.e., when $Z_{in} = Z_s^*$. Depicted below is the equivalent circuit of a transmit antenna, where the characteristic impedance Z_0 is equal to the antenna input impedance Z_{in} (Figure 2.3). [48]

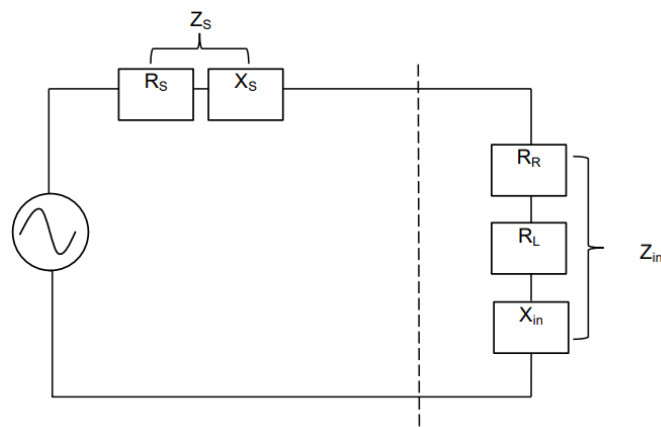


Figure 2.3 Equivalent circuit diagram of a transmit antenna:
 X_{in} - imaginary part of the antenna input impedance and R_R - radiation resistance, R_L - loss resistance comprise the real part of the antenna input impedance [48]

2.2.2 Antenna parameters

An impedance mismatch causing a part of the incident power to be reflected leads to the creation of what is known as standing waves. Standing waves can be characterized by voltage standing wave ratio (VSWR), a parameter that is defined as the ratio of the maximum and minimum voltages on a transmission line. To calculate VSWR, a parameter known as reflection coefficient Γ is commonly used which describes the ratio of the amplitudes of the reflected and incident waves respectively [48]:

$$\Gamma = \frac{V_{refl}}{U_{forw}}, \quad (2.4)$$

where V_{refl} - amplitude of the reflected wave, V,
 V_{forw} - amplitude of the incident wave, V.

Using this coefficient, the VSWR can be calculated as follows [48]:

$$VSWR = \frac{1 + |\Gamma|}{1 - |\Gamma|}. \quad (2.5)$$

Another representation used to describe the incident power reflected due to impedance mismatch is power loss. This parameter can be derived from the reflection coefficient in the following way [48]:

$$a_r = -20 \log |\Gamma| = -20 \log \left(\frac{V_{refl}}{V_{forw}} \right) = -10 \log \left(\frac{P_{refl}}{P_{forw}} \right), \quad (2.6)$$

where a_r - return loss value, dB,
 P_{refl} - reflected power, W,
 P_{forw} - incident power, W.

In addition to the antenna parameters depicted in equations 2.4 to 2.6, the bandwidth of an antenna must be considered. The bandwidth criteria considered in the current thesis relates to the range of frequencies within which the antenna can radiate energy with a return loss greater than or equal to 6 dB. The bandwidth can also be represented in terms of VSWR. Regardless, either parameter can be determined if the other is known using equation 2.6. [47], [48]

For a return loss of 6 dB, or equivalently, a VSWR value of 3, the maximum percentage of power reflected over the frequency range defined here as the bandwidth can be calculated using the formula depicted in equation 2.6:

$$6 \text{ dB} = -10 \log\left(\frac{P_{refl}}{P_{forw}}\right) \Rightarrow \frac{P_{refl}}{P_{forw}} = 10^{-0,6} \approx 0,25 .$$

Thus, over the frequencies within the bandwidth specified by a return loss of 6 dB, at maximum approximately 25% of the incident power will be reflected. In essence, this definition of the bandwidth indicates how well the antenna is matched to the transmission line over the considered frequency band [47].

To determine both the percentage of reflected power over certain frequencies, as well as the consequent bandwidth of an antenna, a vector network analyzer (VNA) can be utilized. This instrument characterizes the S parameter, e.g., the S11, which is an indication of the return loss measured at the input port of the signal. To determine the bandwidth for a specified return loss, the S11 parameter is graphed over a range of frequencies. The S11 parameter relates directly to the return loss, as these parameters are equal in magnitude but have the opposite sign. As the network analyzer connects to the antenna feed, the S11 parameter technically describes the reflection between the VNA port impedance and the network's input impedance. Thus, the value of S11 comprises all the reflection losses caused by impedance mismatches in the network from the port to the antenna. An example representation of the S11 parameter over a range of frequencies obtained with a network analyzer is depicted below (Figure 2.4). [47], [50]

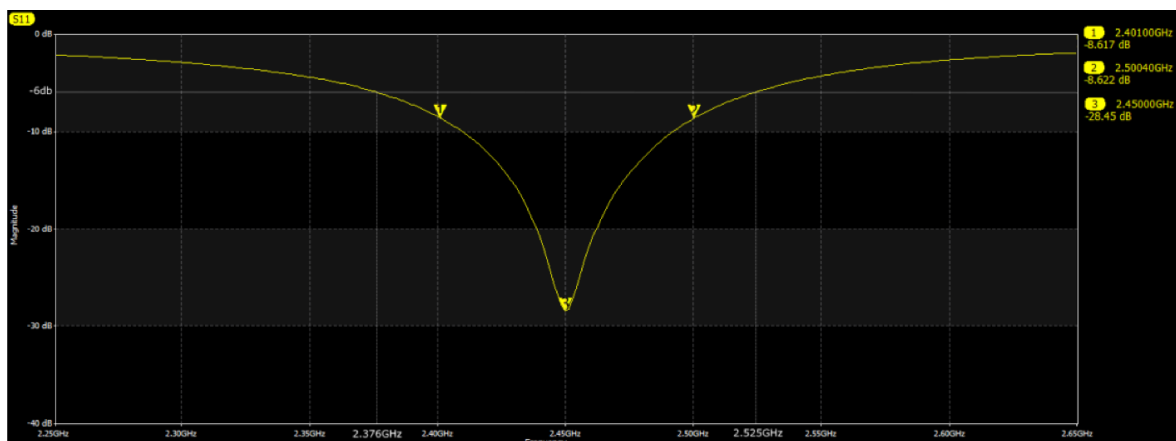


Figure 2.4 Example representation of the S11 parameter measurement with a network analyzer

2.2.3 Impedance matching

As discussed previously, impedance matching is required to maximize power delivery from the source to the load. The objective of impedance matching is to match the source and the load impedances to the characteristic impedance of a transmission line. In an ideal case, the transmission line does not dissipate any energy as its characteristic impedance is only defined by the path's capacitance and inductance. An equivalent model of an ideal transmission line is depicted below (Figure 2.5). [47]

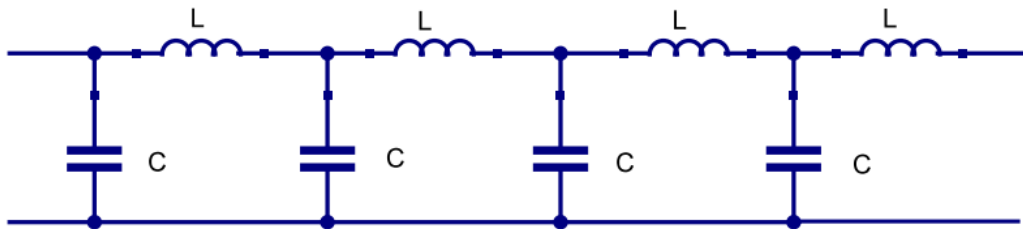


Figure 2.5 Equivalent model of a transmission line [47]

Therefore, the characteristic impedance of an ideal transmission line can be determined with the following equation [47]:

$$Z_0 = \sqrt{\frac{L}{C}}, \quad (2.7)$$

where C - distributed capacitance along the length of the transmission line, F,
 L - distributed inductance along the length of the transmission line, H.

Hence, to match the complex source and load impedances to the characteristic impedance of the transmission line, matching networks comprising a set of inductive and capacitive elements in a combination of shunt and series configurations are used. More generally, a matching network is a circuit consisting of passive elements that is used to transform the load and source impedances to the characteristic impedance of the transmission line. When a matching network is used, it is recommended that it be placed near the source, or the load being matched to the transmission line. This ensures that the matching network component values remain independent from the length of the trace connecting them. [47]

A useful graphical tool in designing a matching network is the Smith chart. This tool enables calculating multiple important parameters, including the return loss, reflection coefficient and VSWR. An example Smith chart is depicted below (Figure 2.6). [47]

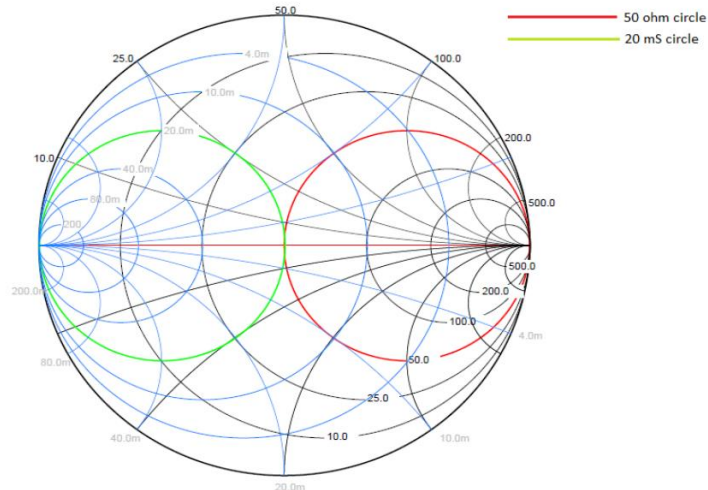


Figure 2.6 An example Smith chart depicting impedance and admittance circles [47]

On the Smith chart, the left corner indicates zero ohms, and the right corner indicates an open circuit. The circles touching the right and the left corner are constant-resistance and constant-conductance circles respectively. The center point of the circle is the characteristic impedance point, which in Figure 2.6 is $Z_0 = 50 \Omega$. This point also corresponds to the 20 mS point, as the red and green circle represent 50 Ω and 20 mS circles respectively. In this example, the first step in matching the impedances is to transform the impedance onto either the 50 Ω or 20 mS circle. Next, the impedance needs to be transformed to the characteristic impedance, i.e., 50 Ω in this case. The impedance can be transformed or moved on the Smith chart by adding a combination of series or shunt inductance and capacitance into the circuit as shown below (Table 2.3). The table describes the effects of inductance and capacitance added to the transmission line between the source and load in shunt and series configurations, the circle on the chart on which the movement occurs, the direction of the movement, and the value of component required to move the reactance by a factor X on the chart. [47]

Table 2.3 Components required for impedance matching on a Smith chart:

L - value of inductance to move the reactance by a factor of X_L , C - value of capacitance to move the reactance by a factor of X_C , f - frequency of the received or transmitted signal. [47]

Component	Configuration	Circle of movement	Direction of movement	Value of component
Inductor	Series	Constant resistance	Clockwise	$L = \frac{X_L}{2\pi f}$
Capacitor	Series	Constant resistance	Counterclockwise	$C = -\frac{1}{2\pi f X_C}$
Inductor	Shunt	Constant conductance	Counterclockwise	$L = \frac{-1}{2\pi f Y_L}$
Capacitor	Shunt	Constant conductance	Clockwise	$C = \frac{Y_C}{2\pi f}$

2.3 Power supply topology selection

The current device has a few important design restrictions that must be considered when selecting the power supply. Namely, this low-power device must work from mains voltage while not generating too much heat, the output needs to be galvanically isolated from the mains, and the power supply must fit on a limited board area. It is therefore apparent that a feasible power supply topology must be selected from a list of isolated switch mode power supply (SMPS) topologies. The basic structures of four such topologies considered are depicted below (Figure 2.7).

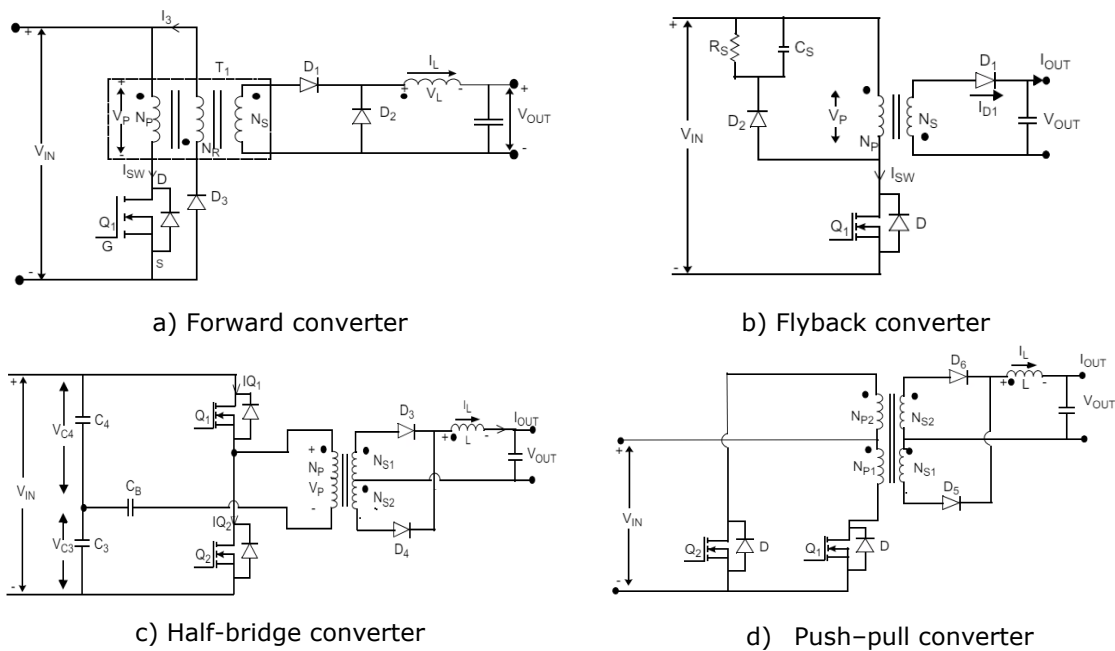


Figure 2.7 Basic structures of different isolated SMPS topologies [51]

Some of key factors considered to select the most optimal isolated SMPS topology for the current application are depicted in the table below (Table 2.4). It is important to note that no specific design examples are considered here, as only the basic structures of these topologies are compared relative to each other.

Table 2.4 Comparison of different SMPS topologies [51], [52], [53]

Topology	Input voltage	Output power	Efficiency	Component count	Cost	Application considerations
Forward converter	Universal (90-264 VAC)	<150 W	Medium	Medium-high	Medium-high	High voltage stress (up to $\geq 2 \cdot V_{in}$) on switch, suited for high load current applications

Table 2.4 Continued

Topology	Input voltage	Output power	Efficiency	Component count	Cost	Application considerations
Flyback converter	Universal (90-264 VAC)	<150 W	Medium	Low	Low	High voltage stress (up to $\geq 2 \cdot V_{in}$) on switch, suited for low-cost, low-power low-volume supplies
Half-bridge converter	Universal (90-264 VAC)	<500 W	High	High	High	Low voltage stress (V_{in}) on switch, suited for high input voltage, higher power applications
Push-pull converter	Universal (90-264 VAC)	<500 W	Medium-high	High	Medium-high	High voltage stress ($2 \cdot V_{in}$) on switch, better suited for 110 VAC system

From Table 2.4, it is evident that the flyback converter is best suited for the current application. While the flyback converter does not provide the best efficiency, the output power demand of this application is relatively low, not exceeding 1 W at any time. Therefore, the design needs to be efficient enough, where the power losses during normal operation do not cause excessive temperature rise inside the junction box. A more restrictive design consideration is the available board space; however, the flyback has the lowest component count of the isolated SMPS topologies. Additionally, the relatively lower cost of the power supply makes the flyback converter compelling in case this device is produced. The high voltage stresses the switching element is exposed to can be resolved by using a snubber circuit and selecting a switch that can tolerate sufficiently high voltages.

2.4 Flyback Topology

The flyback topology is one of many SMPS topologies. The flyback converter outputs one or multiple voltages from a DC input source. When operated from an AC source such as mains voltage, the line must first be rectified to obtain the required DC input into the primary winding of the flyback transformer. A benefit of using the flyback topology is the option to generate multiple output voltages by adding additional

windings to the flyback transformer. The basic structure of the flyback converter comprises a flyback transformer, a power switch, an output diode, and an output capacitor. This general structure in conjunction with the operation of a flyback converter in discontinuous conduction mode (DCM) is depicted in the figure below (Figure 2.8). [52]

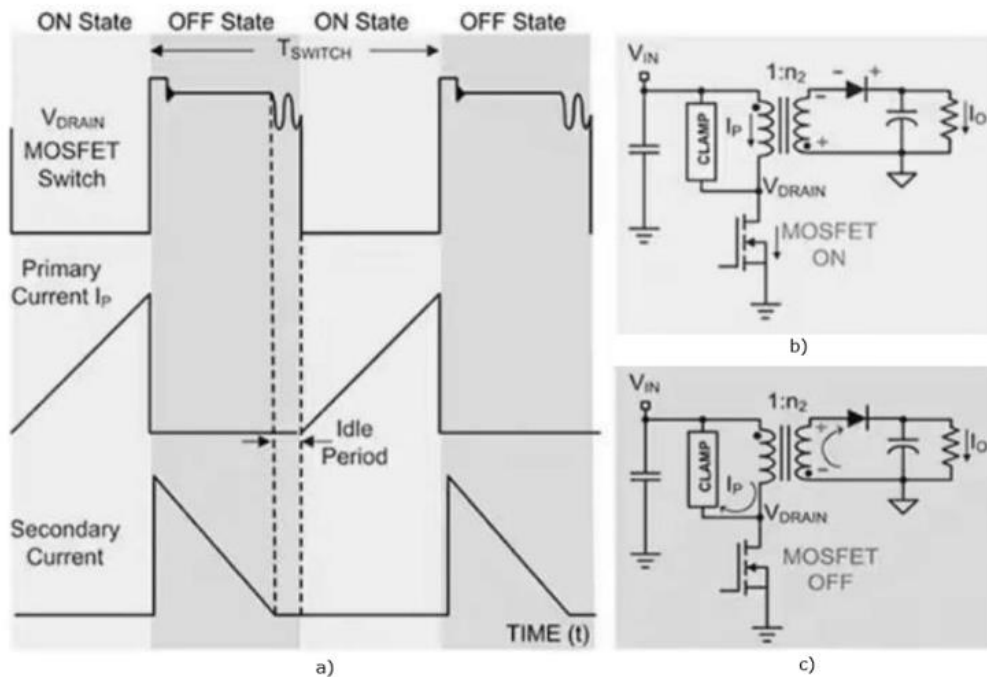


Figure 2.8 a) Operation of a flyback converter in DCM, b) and c) basic structure of a flyback converter and depiction of current flow with switch on and off respectively: V_{in} - input voltage, V_{drain} - voltage on the switch, I_p - current through the primary winding, I_o - output current, $1:n_2$ - turns ratio between the primary and secondary windings, T_{switch} - period of the switching cycle [52]

The central component of the topology, a flyback transformer, operates differently compared to a conventional transformer and is sometimes referred to as a coupled inductor instead. Contrary to a conventional transformer, energy entering the primary winding is not immediately transferred to the secondary but is instead stored in the air gap of the transformer core. The windings of the flyback transformer are wound such that the phases are reversed. Thus, when the switch, e.g., a metal-oxide-semiconductor field-effect transistor (MOSFET) is on (Figure 2.8 b), the primary winding conducts current which rises linearly (Figure 2.8 a). The energy is stored in the magnetizing inductance of the transformer. Meanwhile, the output diode in the secondary circuit is reverse biased and current does not flow through the secondary winding. During this period, the current is supplied by the output capacitor. When the switch is turned off, the diode becomes forward biased (Figure 2.8 c), and the stored energy is transferred to the secondary side to supply the load as well as charge the output capacitor. [52]

In general, three different modes of flyback power supply operation are distinguished. Discontinuous conduction mode (DCM) refers to the converter operation where the secondary current falls to zero and remains there for an idle period (Figure 2.8 a) before the switch is turned on again repeating the cycle. The power converter in the current solution is designed to operate in DCM. Advantageously, DCM allows for using a smaller transformer due to the complete discharging of the energy stored during the on state. Minimizing the transformer's physical dimensions is very important given the stringent constraints on available board space. The second mode of operation is called continuous conduction mode, where the secondary current does not fall to zero before the switch is turned on again. Consequently, the energy stored in the transformer core is never fully discharged. If the converter operates on the boundary of the two aforementioned modes, where the current falls to zero but the switch is turned on immediately after, resulting in no idle period, then the converter operates in what is known as boundary or critical conduction mode. [52], [54]

Due to imperfect coupling between primary and secondary windings, a certain amount of energy is not transferred to the secondary and is stored in the transformer's leakage inductance. When the switch is turned off, this stored energy places high voltage stress on the switch. This voltage on the MOSFET's drain is represented with the symbol V_{drain} in Figure 2.8. To protect the switch, a clamp or a snubber circuit is utilized to limit the maximum voltage on the drain node [52]. The leakage inductance of the transformer and the parasitic capacitance of the switch, e.g., drain to source capacitance of a MOSFET, form a resonant circuit causing an oscillation of energy stored in the leakage inductance. This energy is stored while the switch is on, and the primary winding conducts current. Its value can be calculated with the following equation:

$$E_{lk} = \frac{L_{lk} \cdot I_{p,max}^2}{2}, \quad (2.8)$$

where E_{lk} - energy stored in the leakage inductance, J,

L_{lk} - value of the leakage inductance, H,

$I_{p,max}$ - maximum primary current, A.

As the switch is turned off, the current charges its parasitic capacitance and the voltage on the drain node increases as described by the following equation:

$$E_{lk} = \frac{C_{ds} \cdot V_{ds}^2}{2} \Rightarrow V_{ds} = \sqrt{\frac{2 \cdot E_{lk}}{C_{ds}}}, \quad (2.9)$$

where E_{lk} - leakage inductance energy transferred to the parasitic capacitance, J,
 C_{ds} - value of the parasitic capacitance, F,
 V_{ds} - voltage on the drain node, V.

The frequency of this oscillation caused by the resonant circuit is calculated in the following way:

$$f_{osc} = \frac{1}{2 \cdot \pi \cdot \sqrt{L_{lk} \cdot C_{ds}}}, \quad (2.10)$$

where f_{osc} - frequency of oscillation.

This resonance can be observed during idle time in DCM, and as a damped voltage oscillation on the drain node swiftly after the switch is turned off. After the energy stored in the leakage inductance has been dissipated, the voltage on the switch will remain at a higher value than the initial input voltage. This is caused by the coupling between the primary and secondary windings, as an additional reflected voltage will be added to the input voltage. The value of the reflected voltage is determined by the turns ratio between primary and secondary windings and can be calculated in the following way:

$$V_{Reflected} = V_{Secondary} \cdot \frac{N_1}{N_2}, \quad (2.11)$$

where $V_{reflected}$ - voltage reflected from the secondary to the primary winding, V,
 $V_{secondary}$ - output voltage of the secondary winding, V,
 N_1 - number of turns in the primary winding,
 N_2 - number of turns in the secondary winding.

The maximum voltage applied to the drain node right after the switch is turned off can then be determined from the following equation:

$$V_{drain,max} = V_{AC,RMS} \cdot \sqrt{2} + V_{Reflected} + V_{ds}, \quad (2.12)$$

where $V_{drain,max}$ - maximum voltage observed on the drain node, V,

$V_{AC,RMS}$ – RMS value of the mains voltage, V.

An example oscilloscope image from power supply testing is provided below, depicting the voltage changes on the drain node (Figure 2.9).

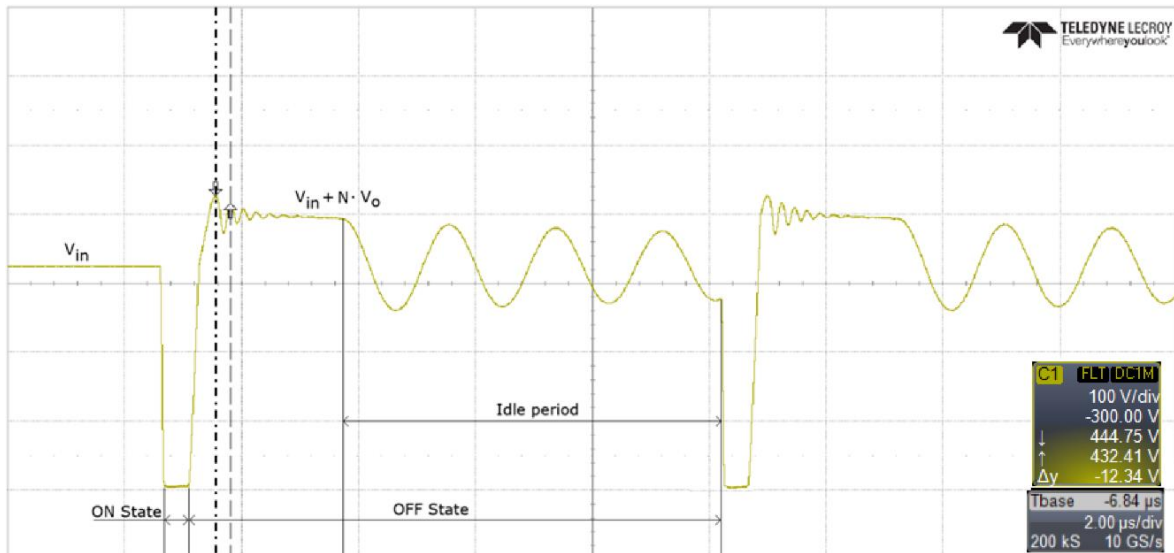


Figure 2.9 Example oscilloscope image of a flyback converter in DCM:
 V_{in} - input voltage, V_o - output or load voltage, N - turns ratio between the primary and secondary windings

To maintain a stable supply output voltage at a desired value, regardless of changes in the load or fluctuations in input voltage, control of the switching element is required. Commonly, a pulse width modulated (PWM) signal is applied to the control element of the switch to regulate the duty cycle of switching. In practice, the switching device is typically driven by a controller. Furthermore, the switching device does not need to be external to the controller package but can also be included with the controller integrated circuit (IC) itself as a multi-chip module. To control the output voltage, two regulation methods are generally implemented. [52]

Primary-side regulation (PSR) is a method where the flyback transformer's auxiliary winding output, which supplies power to the flyback controller, is utilized to regulate the system. In an ideal case, the output voltages of the auxiliary and secondary winding are directly related as determined by the known turns ratio. However, this is not the case in practice, as flyback transformers often suffer from poor cross regulation caused by their imperfect construction. Thus, the output voltage regulation varies to an extent depending on the load condition. [55]

Secondary-side regulation (SSR) allows for more accurate regulation, as the output voltage is sensed directly. Consequently, this method was also utilized in the current application. An optocoupler is used to transmit the signal from the converter output to the controller without breaking the isolation barrier between primary and secondary sides. The basic structures of both regulation methods are depicted in the figure below (Figure 2.10). [55]

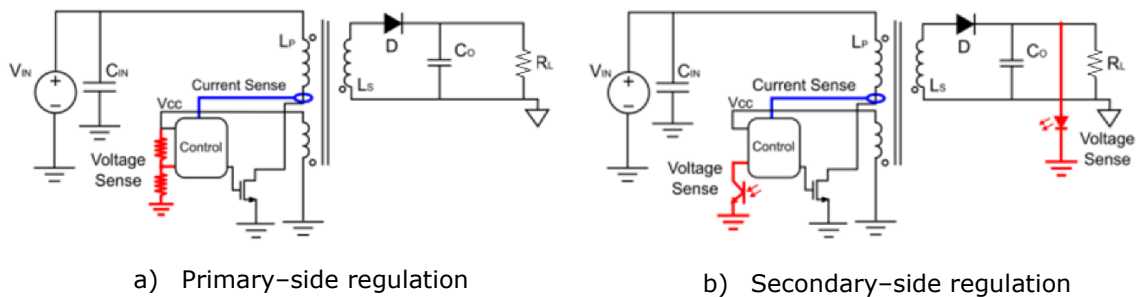


Figure 2.10 Circuits depicting the regulation methods of a flyback converter [55]

3 DEVELOPMENT OF THE SENSOR BOARD

The current chapter pertains to the design of the sensor board. This includes establishing the size constraints on the printed circuit board (PCB), selecting a suitable chip antenna, and designing the antenna circuit. The sensor board comprises a carrier PCB that contains the IAQ sensors, as well as a small radio module for wireless communications that is assembled onto the carrier. The IAQ sensors used in this project were specified by the customer company to assess key environmental and air quality parameters, such as temperature, relative humidity, carbon dioxide, and the concentration of total volatile organic compounds. The first step in the sensor board design process was to determine the dimensional constraints considering the available space inside a common junction box, and the board space required to fit the sensors and radio module. Next, a suitable chip antenna was selected based on comparative tests using a vector network analyzer. The selected antenna's performance is verified on the finalized radio module.

3.1 Physical constraints on the system

As specified by the customer company, the device must fit inside a common junction box. This specification sets constraints on the device's physical dimensions; however, it enables the device to be installed in a range of destinations, e.g., in place of electrical socket-outlets. According to the Certification of Electrotechnical Equipment (CEE) 7 European standard [56], a junction box for a CEE 7 standard electrical socket has a screw spacing of $60 \pm 0,5$ mm with an inner diameter and depth of at least 54 mm and 40 mm respectively (Figure 3.1).

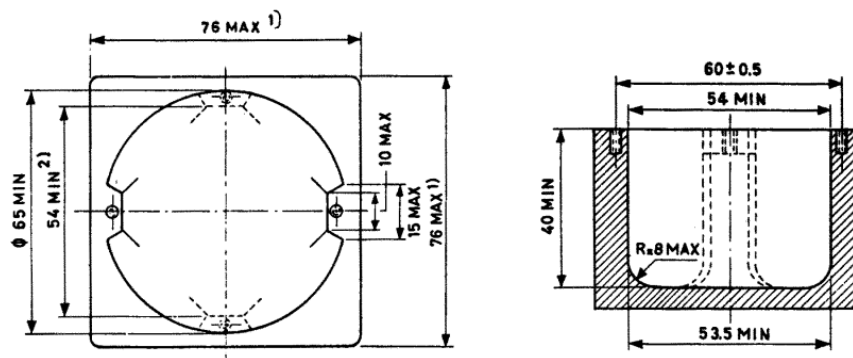


Figure 3.1 Drawing from standard EVS 873_2014 depicting a CEE 7 XIII junction box for a standardized electrical socket, all measurements are in millimeters
The maximum 1) and minimum 2) parameter values are specified from the top of the junction box to a depth of 10 mm and 32 mm respectively [56]

Considering these dimensions, the board area was maximized by setting both the board length and width to 40 mm with a corner radius of 3,25 mm. The rounded corners decrease the diagonal length to not exceed the minimum inner diameter of 54 mm. While the minimum diameter is generally a concern only around the screws where the plastic protrudes, the extra space between the PCB and the inside of a junction box provides ease of installation and leaves room around the device for a frame required for installation. An illustration of a junction box with 60 mm screw spacing and a PCB with the selected dimensions centered inside the box below depicts its fit (Figure 3.2).

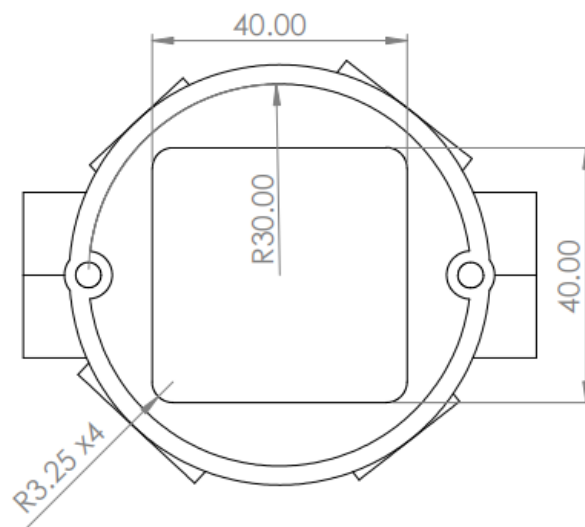


Figure 3.2 Representation of a PCB with selected dimensions centered inside a junction box with 60 mm screw spacing

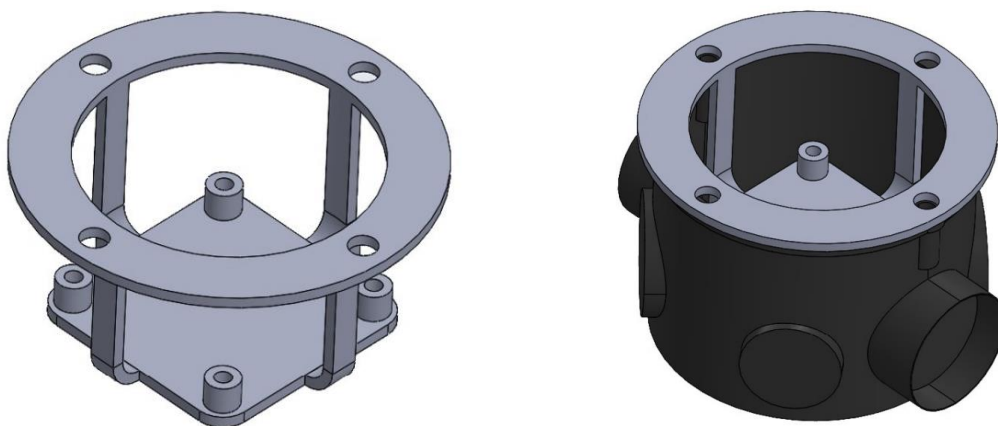
Next, the height constraint on the assembled device must be determined considering the 40 mm minimum depth of a standard junction box depicted in Figure 3.1. The sensor board cannot function independently, as it requires a dedicated power supply to operate. Due to the limited space inside a junction box, the sensor board can only be assembled on top of the power supply PCB using pin headers to connect the boards both electrically and mechanically. However, this later becomes a restricting factor when selecting power supply components as available space is now further limited vertically. To determine the available space, a few factors must be considered. First, some space must be reserved beneath the device for mains wires entering the junction box. Second, the total thickness of the two circuit boards must be considered. Third, the device requires a frame to hold the circuit boards in place and enable installation inside the junction box. Thus, the thickness of the frame's platform also needs to be considered. Lastly, space for small air gaps should be reserved between the power supply components and the sensor board, as well as the underside of the power supply and the platform of the frame. The table below depicts the estimated values for these parameters (Table 3.1).

Table 3.1 Estimation of the total vertical space reserve required inside the junction box

Considered parameter	Value, mm
Total vertical space inside the junction box	40
Space reserved for mains wires	10
Total thickness of the circuit boards	3
Thickness of the frame's platform	2
Space for air gaps	2
Total space for device in the junction box	23

Based on these considerations, the total height of the device, excluding the mounting frame, was allocated a budget of 23 mm. This is equal to the sum of heights of the tallest components on each side of both boards. As it pertains to the sensor board, all components will be mounted on the top side away from the power supply which generates heat during its operation. Given that the sensors were specified by the customer company, the tallest component on the sensor board is predetermined. This is a sensor with a maximum specified height of 6,8 mm, leaving a total of 17,2 mm of space vertically for the components on the power supply PCB.

To mount the circuit boards inside the junction box, a preliminary design for a plastic frame was created. The frame features a washer-like top part with four holes. This enables the frame to be connected to the junction box with screws in four different positions of 90° increments. The bottom part of the frame is a platform with four mounting bosses. These are used to fix the circuit boards in place using plastic screws. The exact height of the mounting bosses can be determined after power supply component selection is finalized. The preliminary design of the frame is depicted in the figure below (Figure 3.3).



a) Preliminary design of the frame

b) Frame mounted inside a junction box

Figure 3.3 Preliminary design of a plastic frame to mount the circuit board assembly

3.2 Design of the antenna circuit

The first step in the design of the antenna circuit is the selection of a suitable antenna. As the radio module is just 18,5 mm in length and 13,5 mm in width, the primary limiting factor in this selection is the antenna's physical size. The total available area allocated for the antenna on the module is a rectangular area of 6 mm length and 7 mm width, centered at the top of the module's smaller edge. Thus, only chip antennas were considered in this case as their small form factor enables their use in applications with limited PCB size [47]. Additionally, using off the shelf components with information about their performance characteristics streamlines the design process when compared to creating a custom PCB trace antenna. Thus, the chip antenna is preferred in this particular case. However, it is important to note that chip antennas require a copper cut-out or clearance area underneath them, which is typically larger than the chip itself. Therefore, the cut-out areas recommended by the manufacturer of each compared antenna were considered for preliminary elimination of antennas that would not fit given the space allocated.

This device utilizes ZigBee-based wireless communication, operating in the 2,4 GHz industrial, scientific, and medical band. ZigBee has a total of 16 channels, i.e., channels 11 through 26, each of which has a bandwidth of 2 MHz with 5 MHz of separation between channels [57]. Therefore, the selected antenna must at minimum provide the bandwidth at the required power output to operate in this frequency range while also accounting for some margin to reduce the effects of detuning. The bandwidth corresponding to the frequency range specified with a minimum return loss value of 6 dB was considered for initial comparison of antennas. Additionally, factors such as the price and available stock of each antenna were noted. Documentation provided by the manufacturer of each antenna was examined to determine if adequate information about their operation and relevant specifications, e.g., radiation pattern and mounting considerations were presented. Considering the aforementioned criteria, four antennas that appeared most viable were selected for testing (Table 3.2). The selection was only limited to four prospective chip antennas, as each antenna requires a specific test PCB, resulting in longer design times and increased design related costs.

Table 3.2 Comparison of preliminary antenna selection parameters of the selected chip antennas

Antenna number	Cutout size (length x width)	Manufacturer estimated bandwidth at a return loss value of -6 dB	Matching, tuning	Unit price at quantity of 100
A1	4 x 6 mm	230 MHz	PI-network	0,7 €
A2	6 x 4 mm	300 MHz	PI-network	0,39 €
A3	6 x 5 mm	250 MHz	PI-network	0,38 €
A4	3 x 5 mm	210 MHz	PI-network, frequency tuning possible	0,45 €

It is important to note, however, that the bandwidth values estimated from the graphs provided in the datasheets are only true for a certain set of conditions that were present when the manufacturer conducted their tests. These include factors such as the methodology of the conducted tests, the exact placement of the antenna on the PCB, as well as the PCB stack-up and size. Moreover, the performance of a chip antenna significantly depends on the ground clearance around the antenna, its placement to achieve optimal radiation, the design of the antenna feed, and the matching network used [47]. Thus, the manufacturer provided bandwidth values were only observed as an indicator of performance, considering that they do not necessarily reflect the actual performance in the current application.

3.2.1 Design considerations

To test each antenna's performance, small boards with dimensions identical to the communication module were designed. Additionally, carrier boards identical in size and shape to the sensor board were created to emulate its influence on the antenna's operation. Both the antenna and the carrier boards were only used during testing and served no further purpose. Unlike the final radio module, the antenna boards only contained the components necessary for the operation of the antenna and the rest were omitted. Thus, each antenna PCB comprised a chip antenna and a U.FL type connector for the connection to the network analyzer. Layout examples from datasheets were considered to choose the placement of the antenna on the PCB, as well as the size of the copper clearance underneath the antenna. To illustrate the designed antenna boards, images of the PCBs for each antenna model are depicted below (Figure 3.4)

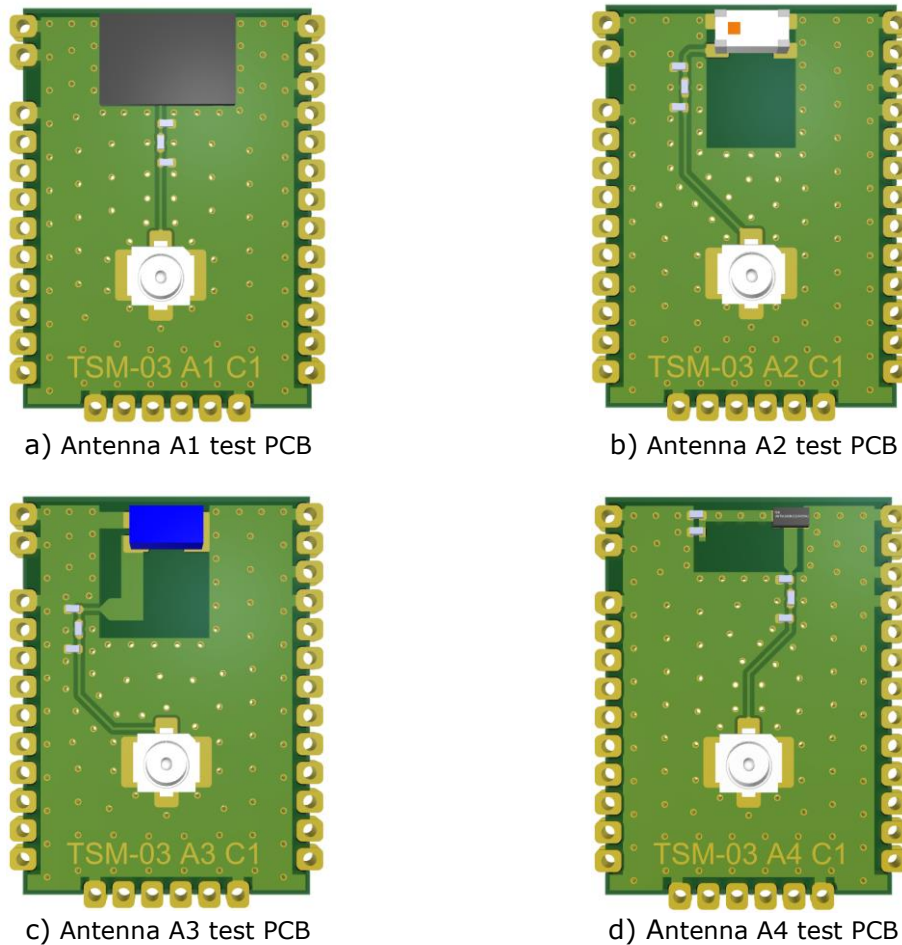
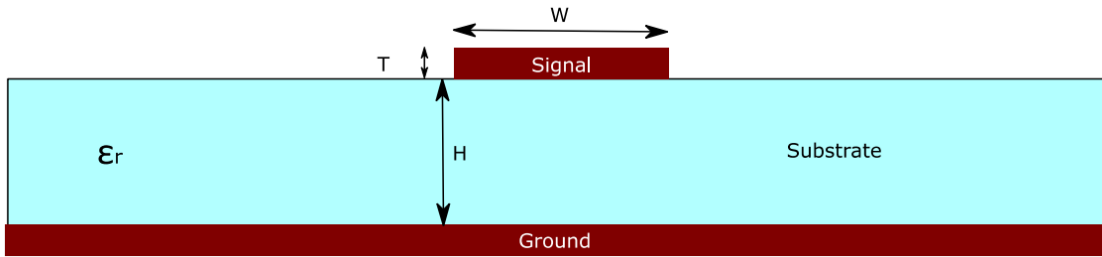


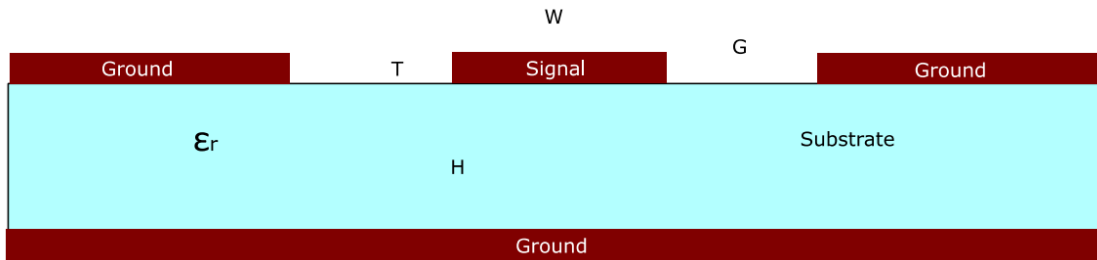
Figure 3.4 An illustration of the antenna boards created for antenna testing

3.2.2 Antenna feed

A very significant factor regarding the radio module's performance, especially at higher frequencies, is the antenna feed. The objective in the current design was to create a feed line with a characteristic impedance of 50Ω . To design the antenna feed, the type of transmission line first had to be selected. Two types of transmission lines generally used for higher frequency applications on PCBs are the microstrip line and coplanar waveguide (CPWG) which are depicted in the image below (Figure 3.5) [47].



a) Cross-sectional view of a microstrip line



b) Cross-sectional view of a CPWG with a bottom/reference ground plane

Figure 3.5 Depiction of the cross-sections of a microstrip line and a CPWG type transmission line: W - width of the feed line, T - thickness of the feed line, H - substrate height, ϵ_R - dielectric constant of the substrate, and G - gap between the feed line and adjacent ground planes [47]

In this application, it was decided to design a CPWG type transmission line due to its advantages, including better isolation for the feed line, easier grounding of shunt elements on the feed line, and reduced crosstalk with other traces compared to a microstrip line [47]. The characteristic impedance of a CPWG depends on the parameters depicted on Figure 3.5 b). Hence, these parameters are the variables that can be selected by the designer such that the feed line obtains the required characteristic impedance. However, in this case the PCB stack-up of the radio module is specified by the customer company. Thus, all parameters except for the width of the feed line and the gap between antenna feed and adjacent ground are predetermined. To calculate these parameters to achieve the required characteristic impedance, a free transmission line calculation software TX-LINE from Cadence was used [58]. An image of the calculator with the parameters entered is depicted below (Figure 3.6).

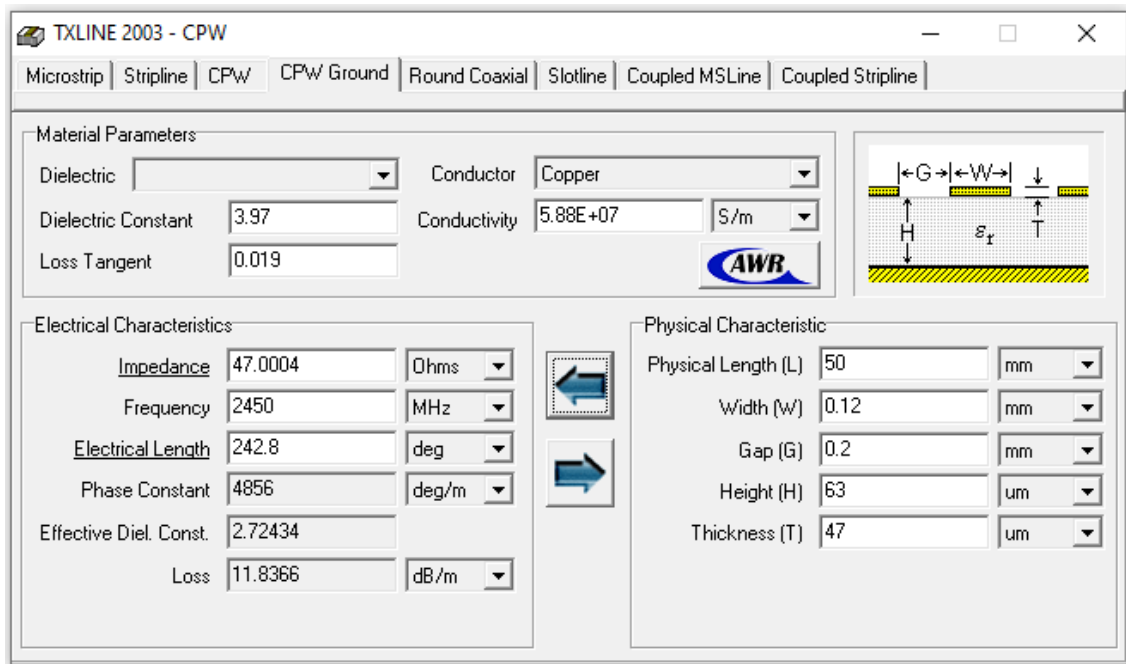


Figure 3.6 Impedance calculation using TX-LINE software [58]

It is important to note that the dielectric constant and loss tangent values were entered manually considering the prepreg material Panasonic's R-1650V used by the PCB manufacturer. This is the dielectric material used between the top copper layer and its closest reference ground layer. These values were obtained from a specification [59] describing the material's properties given the frequency of the transmitted signal, as well as the thickness of the prepreg material.

As can be seen in Figure 3.6, the calculated characteristic impedance for the selected parameters is approximately 47Ω instead of the desired 50Ω . If the track width were to be designed exactly, given that the other parameters remain unchanged, the feed line would have to be approximately $106 \mu\text{m}$ wide according to the TX-LINE calculator. However, it is important to mention that due to the PCB manufacturing tolerances, the width of the track drawn using a computer aided design (CAD) software does not exactly correspond to the width of the actual track on the PCB. The PCB manufacturer specifies that the width of a track will at minimum decrease by the thickness of the base foil, i.e., by at least $12 \mu\text{m}$ for the current stack-up, due to the declension of tracks during the etching process [60]. As the track width decreases, the impedance will increase, thus compensating for the slightly lower impedance. Moreover, the length of the feed line from the U.FL connector to the antenna is relatively small compared to the wavelength of the signal. Given the substrate material, and the frequency of a transmitted signal, its wavelength can be calculated using the following equation:

$$\lambda = \frac{c}{f\sqrt{\epsilon_R}}, \quad (3.1)$$

where λ - wavelength of the transmitted signal, m,
 c - speed of light in vacuum, m/s,
 f - frequency of the transmitted signal, Hz,
 ϵ_R - dielectric constant of the substrate.

The power of a high frequency signal is transmitted as an electromagnetic field. Although most of the field is contained between the copper layers in the substrate, a part of the field exists in the air as well [47]. Given that the dielectric constant of air is 1, the effective dielectric constant for the transmission line is consequently less than what is given for the substrate individually. However, to obtain an approximate value for the wavelength of the transmitted signal, the dielectric constant can be set equal to the value specified by the material's datasheet. For this calculation, the signal frequency value is set to 2,45 GHz, which is close to the center frequency of the ZigBee band. Substituting these values into equation 3.1, the value of the wavelength can be calculated as follows:

$$\lambda = \frac{3 \cdot 10^8 \frac{m}{s}}{2,45 \cdot 10^9 \text{ Hz} \cdot \sqrt{4,0}} \approx 6,12 \text{ cm} .$$

Depending on the specific antenna test board, the feed line has a length between one tenth and one eighth of the calculated wavelength λ . Thus, the length of the transmission line is relatively small compared to the wavelength and should not cause any significant power loss even in the case of a slight impedance mismatch.

3.3 Antenna testing

The selection of a viable antenna model is based on comparative tests measuring the S11 parameter to determine the specified bandwidth for each antenna. Using the LibreVNA, the S11 parameter of each antenna model was observed over a frequency range of 2 GHz to 2,8 GHz. The antenna boards assembled on to their carriers were connected to the LibreVNA via a coaxial cable suspending them in the air, away from objects that could interfere with antenna's operation (Figure 3.7). The setup was not changed over the course of testing different units to obtain comparable results. Initially,

no matching components were added to observe if baseline conditions would provide satisfactory results, as minimizing the component count on the radio module is preferred if possible. Thus, a zero-ohm resistor was used as a jumper in place of the series RF inductor in the antenna feed circuit.

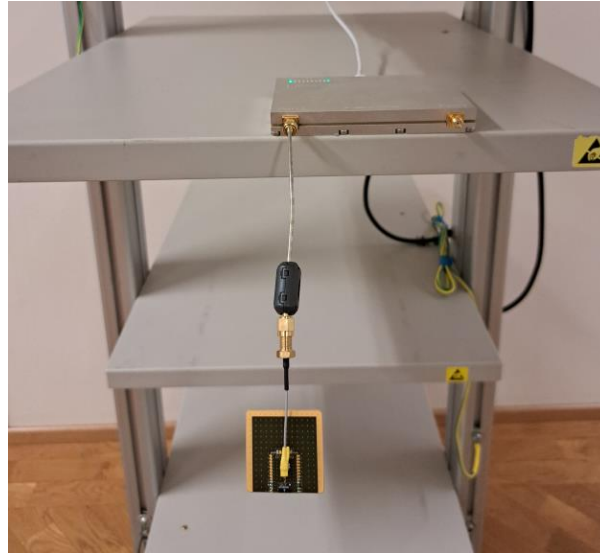


Figure 3.7 Antenna board S11 measurement setup using LibreVNA

3.3.1 Network analyzer test results

The observed bandwidths corresponding to a return loss of 6 dB for each antenna model are presented in the table below (Table 3.3).

Table 3.3 Baseline test results obtained for each antenna model, where frequency low and high indicate the lower and upper bound of the bandwidth respectively. The bandwidth was specified by a return loss of 6 dB, or equivalently, a S11 value of -6 dB

Antenna Board	Frequency Low (MHz)	Center Frequency (MHz)	Frequency High (MHz)	Bandwidth (MHz)	S11 at Center Frequency (dB)
TSM-03 A1 C1	2376	2450	2525	149	-28,5
TSM-03 A2 C1	2256	2360	2450	194	-14,5
TSM-03 A3 C1	2440	2526	2618	178	-26,2
TSM-03 A4 C1	2438	2493	2534	96	-29,5

It is assumed that most of the power transmitted from the VNA was radiated, as no matching components potentially introducing resistive losses were included. Using equation 2.6, it is evident that less than 1% of the incident power is reflected for S11 values lower than -20 dB:

$$\frac{P_{refl}}{P_{forw}} = 10^{-2} = 0,01$$

Thus, comparison of the obtained S11 values at center frequencies is not purposeful, as differences between the total power loss for all antennas, excluding antenna A2, are marginal. However, it can be observed that the center frequencies for all antennas except A1 are significantly shifted from the desired resonance frequency of 2,44 GHz, which approximately corresponds to center frequency of the ZigBee band. Moreover, a frequency shift will occur when the device is placed inside a junction box, as this increases the circuit's effective capacitance causing the resonant frequency to decrease [47]. This effect was also observed during VNA testing, as the center frequency shifted by approximately 20 to 30 MHz when the antenna boards were placed inside a plastic junction box. Hence, the observed resonant frequency of each antenna without matching components is imperative, as three of the four antennas do not feature a frequency tuning network capability to shift the resonance frequency. Furthermore, in the current test conditions, neither antenna A2 nor A3 provide a large enough bandwidth to completely compensate for their respective resonant frequencies falling largely outside the Zigbee frequency range. As antennas A1 and A4 produced better outcomes, antennas A2 and A3 were omitted from further consideration.

Antenna A4's frequency tuning network enables its resonance frequency to be shifted by adding shunt capacitors to the copper connecting to the antenna's radiator electrode. To aid in selecting tuning components, TDK's chip antenna simulation [61] provides reference values, considering various parameters such as the PCB dimensions, copper clearance size, and the distance of the antenna cut-out area from the nearest board edge (Figure 3.8).

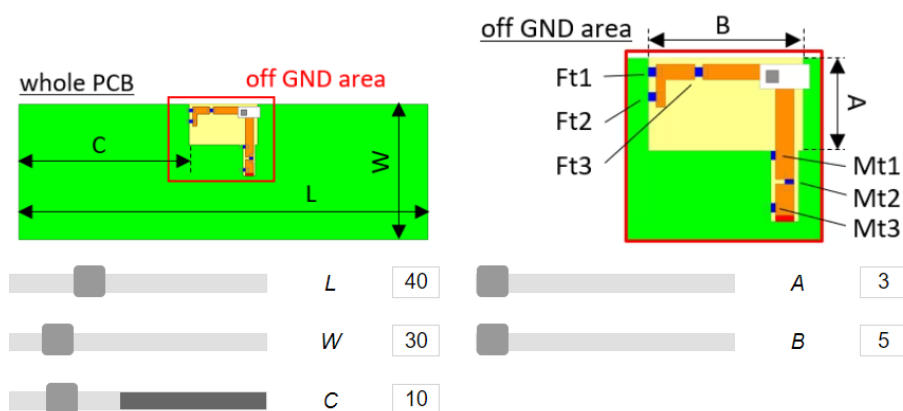


Figure 3.8 TDK chip antenna simulation to determine initial impedance matching and frequency tuning component values:

Ft – frequency tuning components, Mt - impedance matching components [61]

As the exact parameters of the current configuration could not be entered, this simulation was only used for reference. The estimated capacitance value of 7,7 pF obtained with the simulation after entering the approximate PCB parameters proved to be slightly lower than required. During testing, it was determined that an *Ft1* capacitance value of 11 pF would provide a resonance frequency near the midpoint of the ZigBee band (Table 3.4).

Table 3.4, S11 measurement results obtained with antenna A4 using frequency tuning capacitor Ft1 with value 11 pF

Antenna Board	Frequency low at S11 of -6 dB (MHz)	Center Frequency (MHz)	Frequency high at S11 of -6 dB (MHz)	Bandwidth (MHz)	S11 at Center Frequency (dB)
TSM-03 A4 C1	2405	2449	2498	93	-22,8

While enabling frequency tuning, antenna A4's bandwidth without impedance matching was significantly smaller compared to antenna A1, making it more susceptible to the effects of detuning. Additionally, using this antenna would require multiple components for both frequency tuning and impedance matching to achieve the desired performance. Conversely, the comparatively large bandwidth of antenna A1 should be able to compensate for the frequency shifts caused by placing it inside a plastic casing. Moreover, sufficient bandwidth was obtained without utilizing an impedance matching network. Thus, better performance can be expected when appropriate matching components are added to the finalized radio module. With these considerations, antenna A1 was selected as the final chip antenna for this device.

3.3.2 Radio module test results

To evaluate the radio module, comparative tests were conducted with a spectrum analyzer comparing the performance of the new radio module with the selected antenna against a reference device provided by the customer company. The latter is a field-tested product that has shown satisfactory results regarding wireless communications. The gain of the reference device has not been characterized; thus, the results of the comparative tests are relative. Nevertheless, obtaining results comparable to or better than the reference device would indicate adequate performance of the radio module in real environments. To obtain the relative radiation patterns, an HP8529A spectrum analyzer and an Aaronia AG HyperLog 4060 measurement antenna were used. To accurately rotate the device under test (DUT) by a specific amount, a remote-controlled turntable was used. The measurement setup is depicted below (Figure 3.9).



a) Antenna horizontal polarization

b) Antenna vertical polarization

Figure 3.9 Radio module antenna performance measurement setup

As shown in Figure 3.9, measurements were performed with the measurement antenna placed both horizontally and vertically. Moreover, three different orientations of the device under test (DUT) were tested to obtain the radiation pattern for all three planes of the antenna. An illustration of the radio module mounted on to its carrier board is depicted below (Figure 3.10).

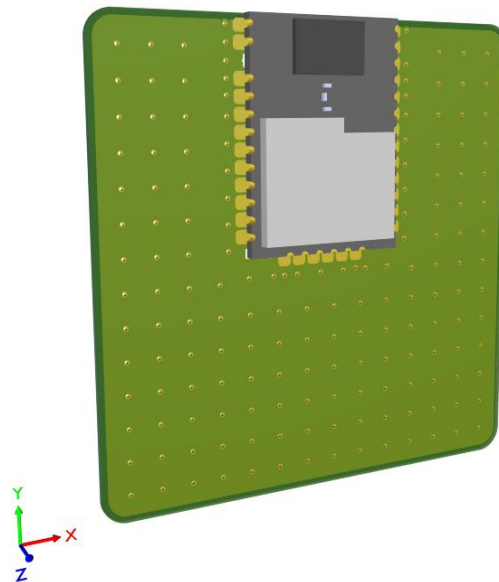


Figure 3.10 Illustration of the radio module mounted on to the carrier board

During tests, both the reference and the current device were oriented in the same way. Thus, the two-dimensional radiation patterns for three planes shown below correspond to the same relative orientation between the axes depicted in Figure 3.10 and the DUT.

The radio module and reference device were set to output a continuous signal with 10 dBm output power. For testing purposes, both devices were programmed to sweep through all 16 ZigBee channels, changing channel every 5 seconds. The turntable rotated the DUT by 30° after each sweep was completed. Consequently, 192 measurements were recorded for each measurement antenna polarization and DUT orientation. While the amplitudes of the received signals slightly differed from channel to channel, the general radiation patterns remained similar. The graphs below depict the relative radiation patterns of the two devices at ZigBee channel 26 for all orientations of the antenna and two measurement antenna polarizations (Figure 3.11 - Figure 3.13).

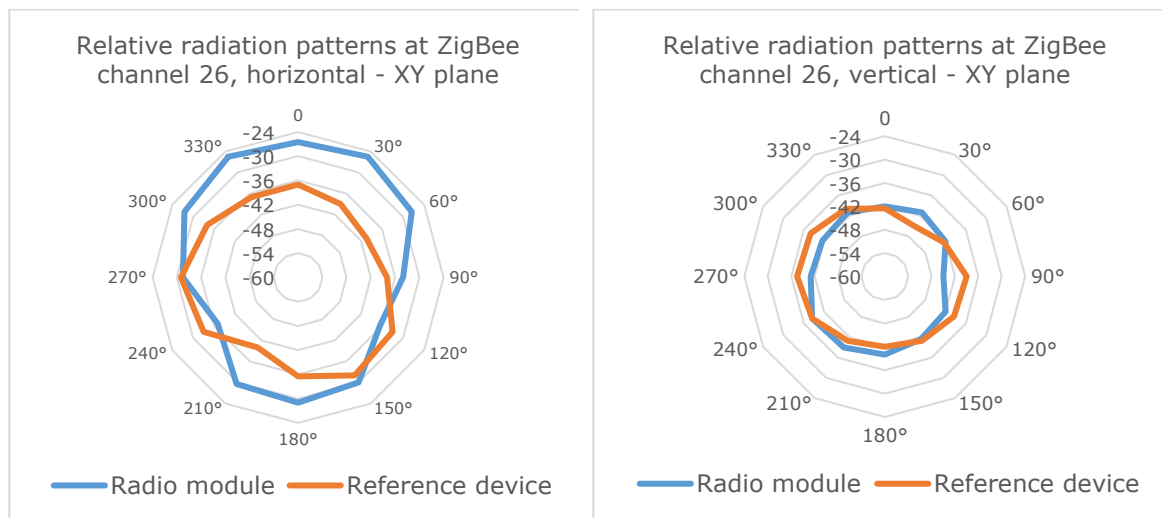


Figure 3.11 Relative radiation patterns of the radio module and the reference device in the XY plane, measurement antenna polarization horizontal (left) and vertical (right), signal amplitude is in dBm

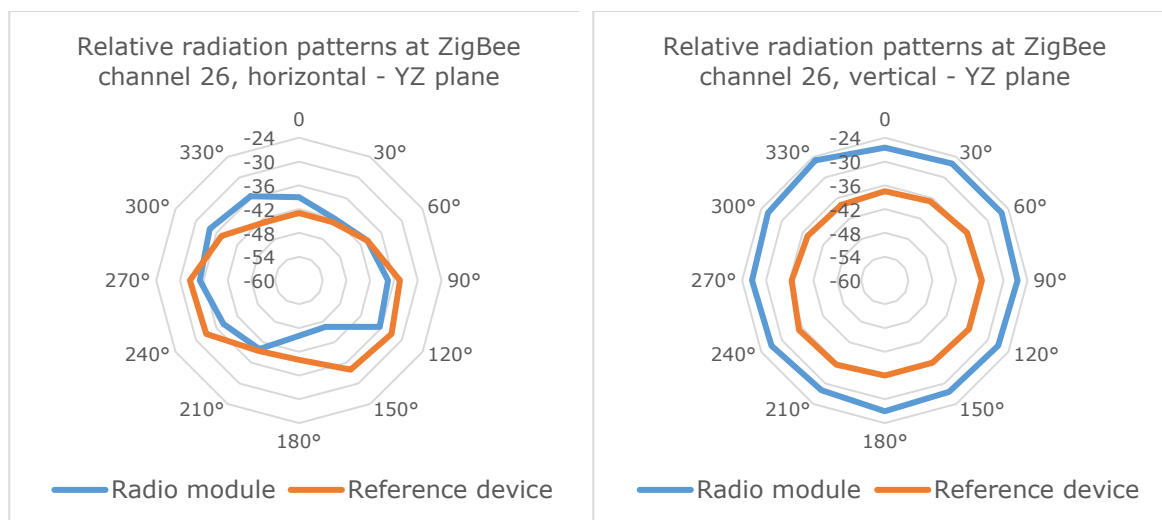


Figure 3.12 Relative radiation patterns of the radio module and the reference device in the YZ plane, measurement antenna polarization horizontal (left) and vertical (right), signal amplitude is in dBm

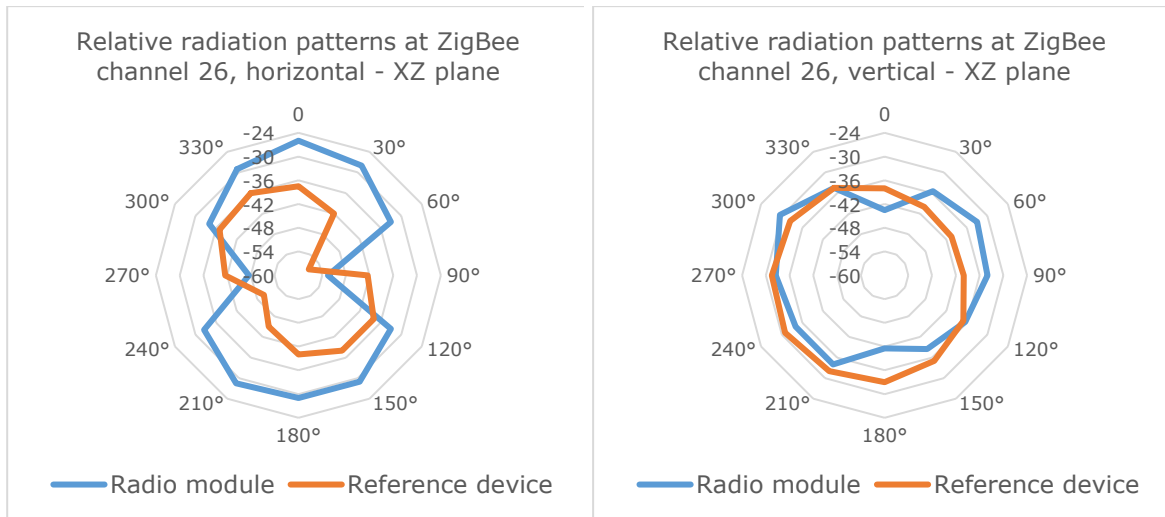


Figure 3.13 Relative radiation patterns of the radio module and the reference device in the XZ plane, measurement antenna polarization horizontal (left) and vertical (right), signal amplitude is in dBm

Results of these comparative tests indicate that the new radio module generally outperforms the reference device in most configurations while also considering the channel-to-channel variations. Moreover, there were no tested configurations where the radio module showed results considerably worse than the reference device. These outcomes provide reasonable confidence in the radio module's performance in real environments, as the reference device is known to function adequately. Nevertheless, further testing could be done to characterize the radio module's performance extensively. For instance, these tests could be repeated in an anechoic chamber while comparing results against a known reference antenna to determine the antenna gain. Furthermore, to determine the true range of reception, the device could be tested in an open outdoor environment clear of any interfering signals present indoors.

4 DESIGN OF THE POWER SUPPLY

The content of this chapter pertains to the design of the IAQ monitor's power supply in flyback topology. One of the key specifications of the developed system is operating from mains power. However, both the radio module and the IAQ sensors used in the current application are designed to work with a relatively low DC supply voltage. On average, the device consumes very little power, as relatively higher power consumption events such as sensor data transmission and IAQ parameter sampling occur infrequently. The power consumption, duration, and frequency of these events are specified by the customer company. Moreover, the operating voltage of the radio module and IAQ sensors are known. Hence, the basic requirements for the power supply can be established (Table 4.1).

Table 4.1 Power supply requirements and specified power consumption of the device

AC input voltage	Required DC output voltages	Average power consumption operating at 3,3 V	Peak output power requirement (total of 3,3 V and 5 V devices)	Maximum no-load voltage ripple at 5 V
Universal, 90-264 V	5 V and 3,3 V	<20 mW	1 W	30 mV

The power supply must provide two output voltages, namely 5 V and 3,3 V. The flyback converter will be designed to output 5 V to supply the environmental sensor with the highest peak and average power demand. This sensor requires the unloaded supply voltage ripple value to remain within 30 mV peak to peak. To provide the 3,3 V supply voltage for the radio module and the other IAQ sensors, a low-dropout regulator (LDO) is added to the power supply PCB. Although the efficiency of LDO is considerably worse when compared to an SMPS, its use is feasible in this case for two main reasons. First, the average current consumption of the devices supplied by 3,3 V is insignificant; thus, the overall efficiency of the power supply will only be reduced marginally. Second, the selected LDO will provide significant ripple rejection from its input to output to supply the more sensitive circuits with a low ripple supply voltage. The peak output power requirement is specified as 1 W; however, this value includes a margin greater than 25% over the actual peak power consumption. Nevertheless, this value is regarded as a specification for the power supply and considered during load tests.

Further design considerations relate to efficiency, board dimensions, and safety. Although this is a low power device, the efficiency of the power conversion must be considered as excessive heat generated by the power supply will interfere with the

operation of the sensors. The component count of the power supply must be kept to a minimum, due to the stringent restrictions regarding available board space. Additionally, safety requirements defined by relevant IEC standards must be followed. The most important aspect of these requirements from the PCB design perspective are minimum clearance and creepage distances.

4.1 Safety Considerations

An important aspect in the design of the device’s power supply is the galvanic isolation between the input and output. As the IAQ monitor is supplied directly from mains, the requirements specified by IEC overvoltage categories (OVC) must be considered. Descriptions of overvoltage categories I to IV as defined in standard [62] are depicted below (Table 4.2).

Table 4.2 Overvoltage categories defined in standard IEC 61558-1 [62]

Overvoltage category	Description
I	“Equipment for connection to circuits in which measures are taken to limit transient overvoltages to appropriately low level” [62]
II	“Energy-consuming equipment to be supplied from the fixed installation” [62]
III	“Equipment used in fixed installations and for cases where the reliability and the availability of the equipment is subject to special requirements” [62]
IV	“Equipment used at the origin of installation” [62]

These categories determine the value of the mains transient voltage, i.e., the largest transient voltage that is expected at the power input of equipment connected to the mains [63]. Mains transient voltage is also a factor in determining the minimum creepage and clearance distances for isolation that must be considered during the power supply design. As is evident from the definitions above, the IAQ monitor belongs to OVC III given that the device is connected directly to mains in a fixed installation.

The applicable mains transient voltage value can be determined from standard [63] given the OVC and AC mains supply voltage. In the current application, i.e., for a root mean square (RMS) AC mains voltage value of 230 V, and OVC III, the mains transient voltage is specified as 4000 V. To determine the minimum clearance and creepage

distances applicable to the flyback converter, parameters such as the working voltage, insulation type, pollution degree, and material group first need to be selected. Working voltage is defined as: “voltage across any particular insulation while the equipment is supplied at rated voltage or any voltage in the rated voltage range under normal operating conditions” [63]. In this application, the AC mains voltage is full wave rectified before being applied to the transformer’s primary winding. Thus, the peak rectified voltage can be calculated as follows [63]:

$$V_{Peak} = V_{AC,RMS} \cdot \sqrt{2}, \quad (4.1)$$

where V_{Peak} – peak rectified DC voltage, i.e., the working voltage, V,
 $V_{AC,RMS}$ – Nominal mains RMS AC voltage value, V.

To provide an additional margin in case the device is used in places with a higher mains voltage value, the RMS value is selected to be 240 V. Substituting this value into equation 4.1, the working voltage, which is also equal to the peak working voltage in the current application, can be calculated:

$$V_{Peak} = 240 V \cdot \sqrt{2} \approx 340 V.$$

Next, the insulation type was selected as reinforced or equivalently, double insulation. The latter comprises both basic and supplementary insulation and provides a higher degree of protection against electric shock [63]. Subsequently, the degree of pollution and material group need to be established to determine the creepage and clearance distances. Considering the application and the device’s intended operating environment, pollution degree 2 is selected. As per standard [62], pollution degree 2 is defined as: “pollution degree in which only non-conductive pollution occurs, except that occasionally a temporary conductivity caused by condensation is to be expected” [62]. The material group selection is based on the Comparative Tracking Index (CTI) of the insulating material. This index classifies insulating materials into groups based on their electrical breakdown properties. In the current case, the material group is not known; thus, the worst case, i.e., group IIIb shall be assumed [63]. Based on these parameters, the minimum clearance can be determined from standard [64], which specifies the minimum clearance for insulation in primary circuits and between primary and secondary circuits. The minimum applicable clearance in the current application is 6,4 mm [64]. The minimum creepage distance for basic insulation based on the RMS working voltage, degree of pollution, material group, and mains transient voltage is

specified by standard [63]. The exact creepage value corresponding to an RMS working voltage of 340 V is not listed; however, linear interpolation between two consecutive values is permitted if the result is rounded to the next higher 0,1 mm increment [63]. Linear interpolation between two tabulated values is done in the following way:

$$x = x_{low} + \frac{(V_{Peak} - V_{low}) \cdot (x_{high} - x_{low})}{V_{high} - V_{low}}, \quad (4.2)$$

where, x is the interpolated creepage value, mm,

V_{low} is the lower voltage value of the two consecutive table values, V,

V_{high} is the higher voltage value of the two consecutive table values, V,

x_{low} is the lower creepage value of the two consecutive table values, mm,

x_{high} is the higher creepage value of the two consecutive table values, mm.

Substituting the RMS working voltage values of 320 V and 400 V, and their corresponding listed creepages into equation 4.2, the minimum applicable creepage distance x at 340 V can be determined:

$$x = 3,2 \text{ mm} + \frac{340 \text{ V} - 320 \text{ V}}{400 \text{ V} - 320 \text{ V}} \cdot (4 - 3,2) \text{ mm} = 3,4 \text{ mm}.$$

It is important to note that this is the minimum creepage distance for basic insulation. To obtain the minimum creepage for reinforced or double insulation, this value needs to be multiplied by a factor of two. Thus, the minimum applicable creepage distance from the input to the output side in the current power supply design is 6,8 mm.

Lastly, to select a transformer with adequate insulation from primary to secondary, the dielectric strength test voltage needs to be determined. As per standard [62], this value must be selected based on the working voltage, type of insulation, and OVC. Again, linear interpolation between two consecutive values is permitted and shall be used as no table value corresponding to an RMS working voltage of 340 V is specified. For OVC III, and a double or reinforced insulation, the dielectric strength test voltage $V_{insulation}$ can be calculated as follows [62]:

$$V_{insulation} = 4200 \text{ V} + \frac{340 \text{ V} - 300 \text{ V}}{600 \text{ V} - 300 \text{ V}} \cdot (5000 \text{ V} - 4200 \text{ V}) \approx 4307 \text{ V}.$$

Thus, the insulation rating between the flyback transformer's primary and secondary windings must be at least 4,3 kV.

4.2 Flyback transformer and controller selection

The first step in designing the power supply prototype was to select the two key components, namely the flyback transformer and controller. Due to the limited board space, the selected controller must be available in a relatively small package. To further save space on the PCB, only flyback controllers with integrated power switches were considered. Another key parameter to consider is the reverse breakdown voltage of the integrated power switch. This switch is subjected to a large voltage stress right as it is toggled to the off state as demonstrated in section 2.4. To diminish the possibility of destroying the switch, the minimum breakdown voltage was selected as 800 V which exceeds the peak working voltage by more than two times to provide a safe margin. Additionally, low standby and light-load power consumption of the converter is desired to avoid generating excessive heat during typical operating conditions. Controller ICs that provide comprehensive information about their operation and performance characteristics are preferred. Some of the parameters considered for the controller selection are depicted in the table below (Table 4.3).

Table 4.3 Key selection parameters of flyback controllers

OVP – output overvoltage protection, OVT – overtemperature protection, OVL – line overvoltage protection, OCP – overcurrent protection, OLFP – open-loop failure protection UVLO – undervoltage lockout

Parameter	Flyback controller model				
	LNK369x	FSL4110LRLX	VIPER06xS	VIPER01xS	VIPER11xS
Supply voltage	5 V - 7 V auxiliary or supplied from drain node	10 V - 27 V auxiliary or self-biased	11,5 V - 23,5 V auxiliary or self-biased	4,5 V - 30 V auxiliary or self-biased	4,5 V - 30 V auxiliary or self-biased
Drain current limitation (typical)	(205 - 287) mA (375 - 535) mA	520 mA	350 mA, adjusting with resistor	120 mA 240 mA 360 mA	370 mA 480 mA 590 mA
Switching frequency (typical)	66 kHz	50 kHz	30 kHz 60 kHz 115 kHz	30 kHz 60 kHz 120 kHz	30 kHz 60 kHz 120 kHz
Switch breakdown voltage	900 V	1000 V	800 V	800 V	800 V
Operating temperature	-40 °C to 150 °C	-40 °C to 125 °C	-40 °C to 150 °C	-40 °C to 150 °C	-40 °C to 150 °C
Fault protection	Current limiting, OVP, OVL, OTP	OLP, OVP, UVLO, OVL, OCP	Current limiting, OTP, OLFP	OCP, OVP, OTP, OLP	OCP, OVP, OTP, OLP
Height	3,68 mm	3,7 mm	1,75 mm	1,75 mm	1,75 mm
Length	9,83 mm	10 mm	5 mm	5 mm	5 mm
Width	9,86 mm	9,9 mm	6,2 mm	6,2 mm	6,2 mm

As can be observed from the table above, the VIPER line flyback controllers are available in a package that is considerably smaller compared to the other models. Since limited board space is a concern in this application, only these ICs are considered further. Advantageously, all listed VIPER series ICs are effectively pin compatible, as the VIPER06 series models feature optional drain current limiting while the other models use the same pin as an optional PWM disable instead. Nevertheless, all these ICs can be used interchangeably on the same prototype board if necessary. Among the considered models, only the VIPER06 series has an evaluation board (EVB) of a power supply designed in isolated flyback topology. Moreover, with width and length of 27,4 mm and 46,3 mm respectively, the EVB is similarly sized to the power supply designed for the current device. Both the datasheet [65] and the EVB application note [66] provide sufficient information on the operation of the IC. Consequently, the VIPER06 series was selected for further testing.

As it pertains to the selection of a viable transformer, the restrictive design constraints significantly limit the number options to consider. First, the transformer's primary winding voltage must be rated for a working voltage of at least 340 V. As was established in the previous section, the dielectric strength test voltage, i.e., the minimum insulation voltage between the transformer's primary and secondary windings, must be rated for at least 4,3 kV. The selected transformer must also contain an auxiliary winding to supply the flyback controller from a lower voltage source to decrease power consumption. Additionally, the transformer's physical dimensions are considered. As was determined in the previous chapter, the total height reserved for the power supply components is at most 17,2 mm. Considering that some of the power supply components will be placed on the underside of the board, transformers with a smaller height dimension are preferred. Lastly, it is important to note that the considered transformer models must be in active production and available at the time of selection. A list of prospective flyback transformers and their parameters is given below (Table 4.4).

Table 4.4 Key parameters of prospective flyback transformers [67], [68]

Parameter	Transformer model			
	WE 750871013	WE 750312723	WE 750811016	WE 750313959
Primary voltage rating	81 VAC to 275 VAC	85 VAC to 265 VAC	85 VAC to 265 VAC	85 VAC to 265 VAC
Secondary voltage rating	5 V	5 V	5 V	12 V
Secondary current rating	0,6 A	1 A	1,2 A	0,25 A

Table 4.4 Continued

Parameter	Transformer model			
	WE 750871013	WE 750312723	WE 750811016	WE 750313959
Dielectric strength (primary - secondary)	4500 VAC	4500 VAC	4500 VAC	4500 VAC
Auxiliary winding voltage rating	15 V	20 V	13,5 V	18 V
Primary winding inductance	1,8 mH	0,925 mH	1,67 mH	1,8 mH
Saturation current (20% rolloff from initial)	350 mA	440 mA	450 mA	290 mA
Height	10,16 mm	10,41 mm	13 mm	10,41 mm
Length	13,72 mm	14,22 mm	16,9 mm	13,72 mm
Width	20,45 mm	20,45 mm	18,8 mm	20,45 mm

It is evident that all considered models are rated for an output power significantly greater than the specified peak power requirement of 1 W. While the saturation currents vary, the selected controller IC enables drain current limitation with a resistor to accommodate for the specific transformer. It is important to note that the selected transformer's auxiliary winding should output at least 11,5 V, which is the minimum supply voltage of the selected controller IC. This eliminates the model WE 750313959 from consideration, since the 18 V auxiliary voltage is specified for an output of 12 V. Given that the output voltage in this application is regulated to a value more than two times lower (5 V), the auxiliary voltage is scaled down by the same factor, leaving it below the minimum required value. As it pertains to the primary winding inductance, it can be observed that one model exhibits a significantly lower value. In general, models with higher primary inductance values are preferred, as higher inductance results in a lower primary winding current rate of change, consequently extending the converter's power switch on time as the drain current limit will be reached slower. Nonetheless, the lower inductance model is included in testing for comparison. The model WE 750811016 has a relatively high primary winding inductance; however, it requires considerably more vertical space compared to the other transformers. Since it has no apparent advantages over model WE 750871013 with relatively similar parameters, it is omitted from further consideration. Therefore, only models WE 750871013 and WE 750312723 were selected for testing. A VIPER06 evaluation board was used initially to record the power supply efficiencies and power loss values under different load conditions for both transformers. For reference, load tests were also conducted with the EVB's original transformer Magnetica 06401.

4.3 Flyback transformer testing

Considering that the selected flyback transformers satisfy the initial selection criteria, the primary target is to determine which model provides the best efficiency, and consequently, the lowest power losses. The flyback converter EVB was subjected to different load conditions ranging from no load to the maximum specified output power requirement of 1 W. The recorded power loss and efficiency values provide a direct comparison between the performance of each transformer, as the tests are conducted on the same board while other variables remain constant. The graphs depicting the recorded values of output power versus power loss (Figure 4.1), and output power versus power supply efficiency (Figure 4.2) are shown below.

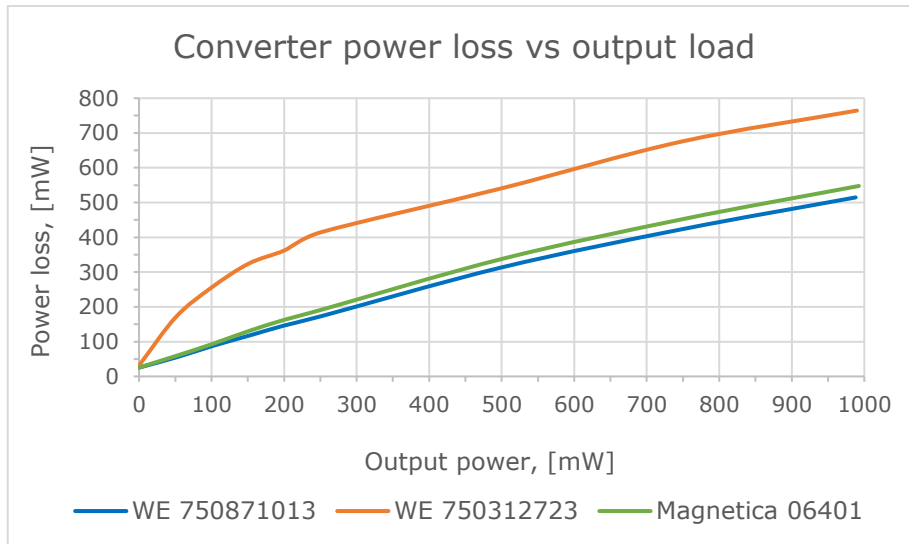


Figure 4.1 Power loss versus output power test results for three different flyback transformers

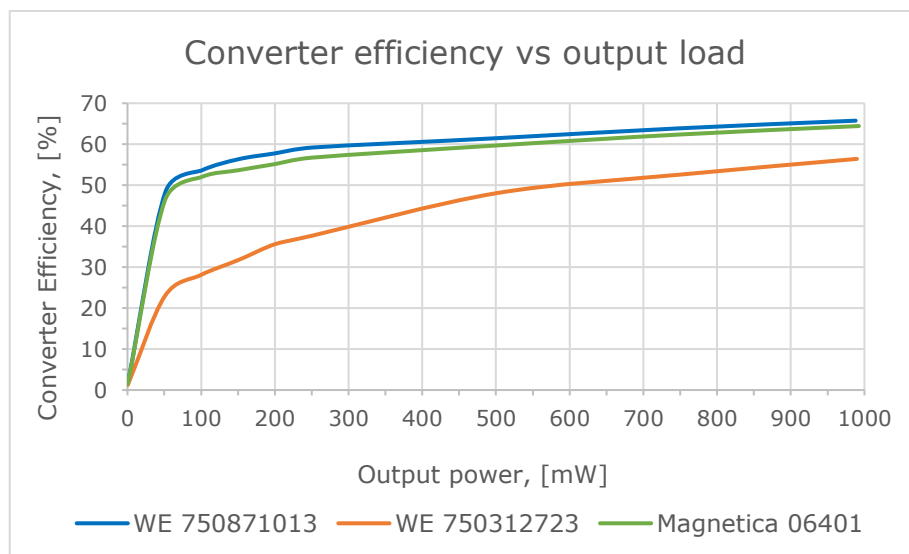
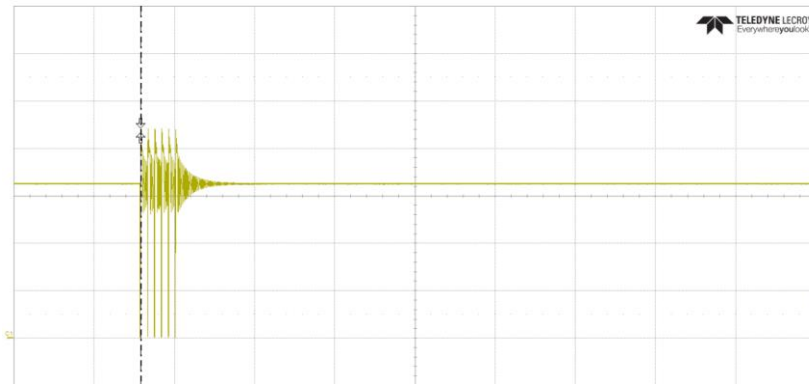


Figure 4.2 Power supply efficiency versus output power test results for three different flyback transformers

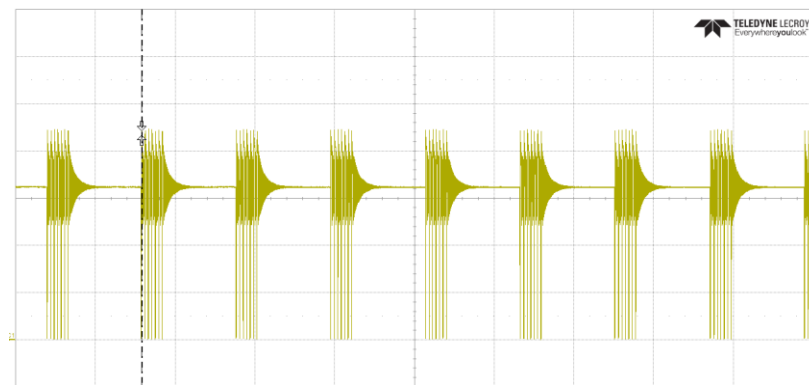
From the graphs above, it is evident that the flyback transformer model WE 750871013 should be selected for the power supply design, as it provided the best results in terms of the considered performance characteristics. Although this outcome was expected, as the primary winding inductance of WE 750871013 is nearly double compared to WE 750312723, an additional factor contributing to increased power losses was the latter's high auxiliary winding voltage. The EVB features an 18 V Zener diode placed on its voltage supply input to protect from overvoltage. A nominal auxiliary voltage value of 20 V will cause a constant flow of current through the Zener diode to clamp this value to the Zener voltage. Nevertheless, the standby and light-load power loss values obtained with the transformer model WE 750312723 are much lower, demonstrating potential to not generate excessive heat during the device's typical operating conditions. All things considered, the EVB tests only function as indicative and the viability of the selected controller IC and transformer model can ultimately be determined after conducting load tests with the power supply prototype.

4.3.1 Operation mode of the flyback converter

To better understand the operation of the converter as the load is changed, the drain node was observed using an oscilloscope. During these tests, the EVBs original transformer was replaced with the selected transformer model WE 750871013. The VIPER06 flyback controllers utilize burst mode control in standby and light-load conditions to limit switching frequency and consequently reduce switching losses. As the name suggests, burst mode refers to the operation of the power converter where the device stops switching for a period of time when the output regulation circuit detects a load low enough for this condition to occur [66]. The oscilloscope images below depict the recorded voltage signal on the drain node during the power converter EVB operation with the selected flyback transformer model in standby and light-load conditions (Figure 4.3).



a) Drain node voltage in standby, time base is 100 μ s



b) Drain node voltage at a load of 250 mW, time base is 200 μ s

Figure 4.3 Oscilloscope recordings of the voltage signal on the drain node in a) standby, b) light-load conditions, vertical divisions are 100 V each on both graphs

It was determined that the converter maintained its operation in burst mode throughout the specified power output range. The converter finally exited this mode when the load was increased to approximately 1,4 W. Therefore, operation outside the burst-mode will not be considered in the current application. It was also noted that while the converter efficiency generally improves as the load is increased, there was no noticeable jump in efficiency right after the converter exited burst mode.

4.4 Thermal considerations

The results of EVB testing provide an estimate of the magnitude of losses in the power supply. Given that the average power consumption of the device is specified, it is now possible to conduct thermal tests to observe the temperature increase inside the junction box during typical operating conditions. This is the primary criterion to determine whether the power supply design is adequate for the current application. A small increase in the temperature of this device during operation is inevitable. However,

it is possible to characterize this parameter in typical indoor conditions to compensate for the temperature increase in software, so the correct ambient temperature values are output. Although there was no specified limit, it was initially estimated that a temperature increase of up to 2 °C inside the junction box over the surrounding environment is a reasonable limit in typical operating conditions. A test wall was constructed to emulate the typical installation of this device. The junction box was thermally isolated from the environment inside the test wall, to simulate a worst-case condition with poor cooling properties. The setup configuration used during this test is depicted in the image below (Figure 4.4).

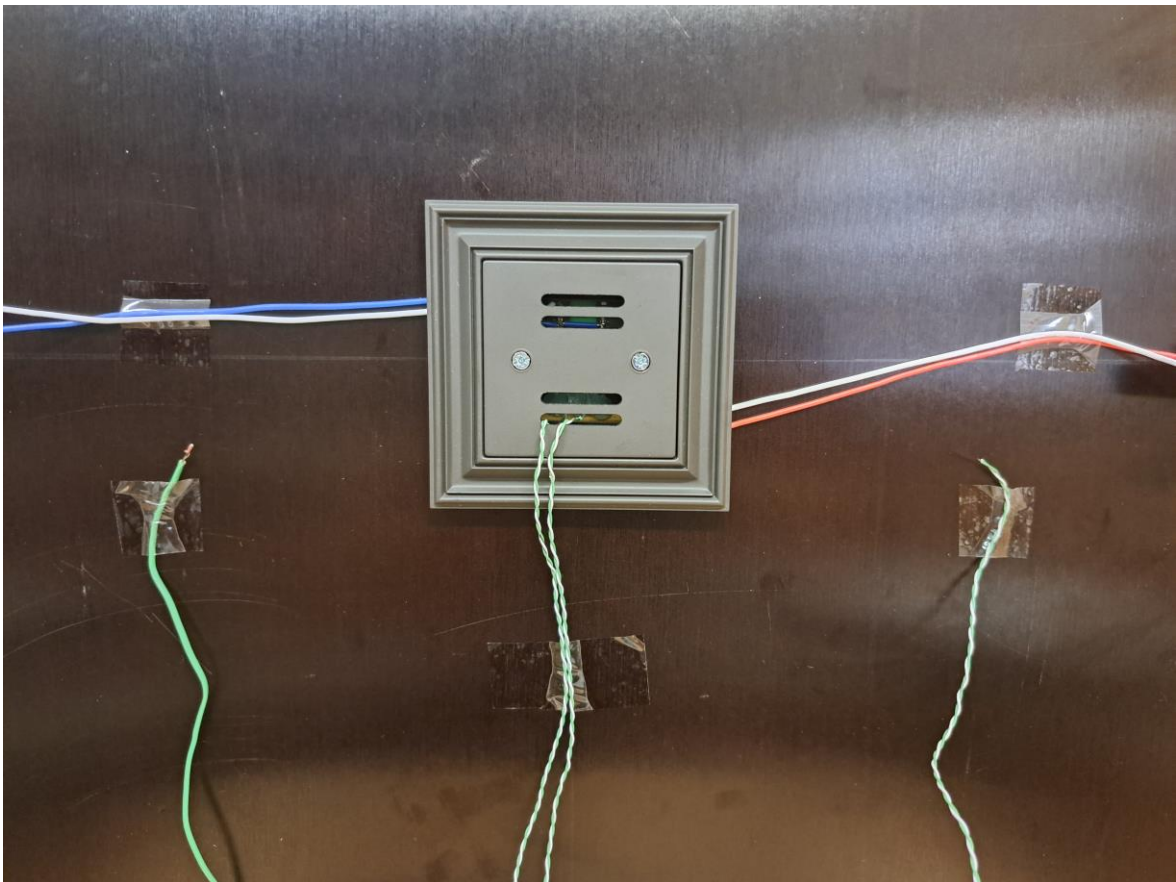


Figure 4.4 Thermal test setup

Behind the blind cover seen on the image above, are two carrier boards mounted to the frame and installed inside the junction box. The boards are assembled using pin headers as described previously. Each board contains a network of resistors spread out over the area of the board. By applying a particular DC voltage to these resistors, it is possible to emulate the power losses of the sensor board and power supply during operation.

$$P_{loss} = \frac{V_{DC}^2}{R_{network}}, \quad (4.3)$$

where V_{DC} – DC voltage applied to the resistor network, V,
 P_{loss} – power dissipated as heat, W,
 $R_{network}$ –equivalent resistance of the resistor network, Ω .

Although the EVB tests provided a reference of the power loss values associated with the power converter, the exact values are yet unknown. Therefore, thermal tests were conducted over multiple points simulating different values of power loss. The power dissipated as heat by the resistor network on the PCB emulating the sensor board was maintained at 20 mW throughout the tests.

Both the ambient temperature and the temperature inside the junction box were recorded using a thermal camera FLIR A655sc. After increasing the power to the next setpoint, the temperature was allowed to stabilize before the values were recorded. An example thermal image of the test setup is depicted below (Figure 4.5).

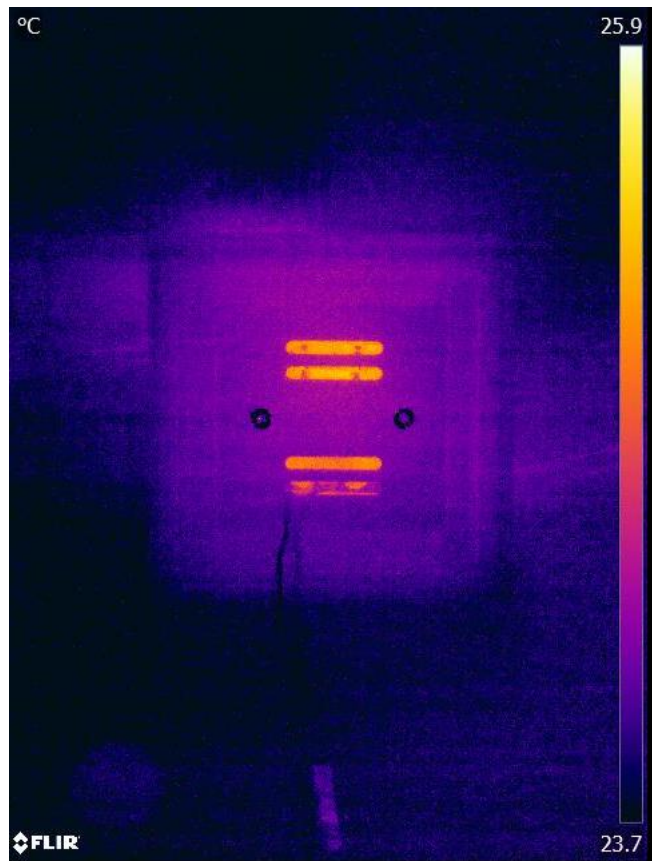


Figure 4.5 Example thermal image captured during testing

It should be noted that the aim of these tests is to determine the difference in temperatures between the device and the environment. Thus, the absolute value of the

temperature indicated by the thermal camera is not important. Temperature values were recorded from inside the junction box through the four slots in the blind cover seen on the image above. Similarly, the ambient temperature was recorded around the blind cover. Using the built in custom area selection and temperature averaging tools of the thermal camera's software, an indication of the temperature increase inside the box was obtained. The results of the thermal tests at different load points are depicted below (Table 4.5).

Table 4.5 Thermal test results

Parameter	Value, mW							
Sensor board power loss	20							
Power supply power loss	30	50	75	100	125	150	200	250
Parameter	Value, °C							
Temperature difference between the junction box & surrounding environment	1,66	1,85	2,09	2,47	2,81	3,18	3,54	4,4

From the table above, it is apparent that there is considerable temperature increase at relatively low power losses. The tests would indicate that power supply losses up to approximately 75 mW during typical operation are acceptable considering the set limit of temperature increase inside the box. Comparing the table values to the EVB power loss obtained at the 20 mW load point, it appears that the selected converter's efficiency is sufficient to provide the required average output power losses within the acceptable range. Therefore, the EVB will be used as a reference to design the power supply prototype for the current device.

4.5 Design of a flyback power supply prototype

The schematic of the power supply prototype is depicted in Appendix 1. At the mains input of the device, an inrush current limiter (ICL) denoted as R1 on the schematic is selected. The ICL used in this application is a fusible wirewound resistor that limits the inrush current caused by the input capacitance when the device is first switched on. A suitable value was determined by simulating the circuit depicted below in LTspice (Figure 4.6).

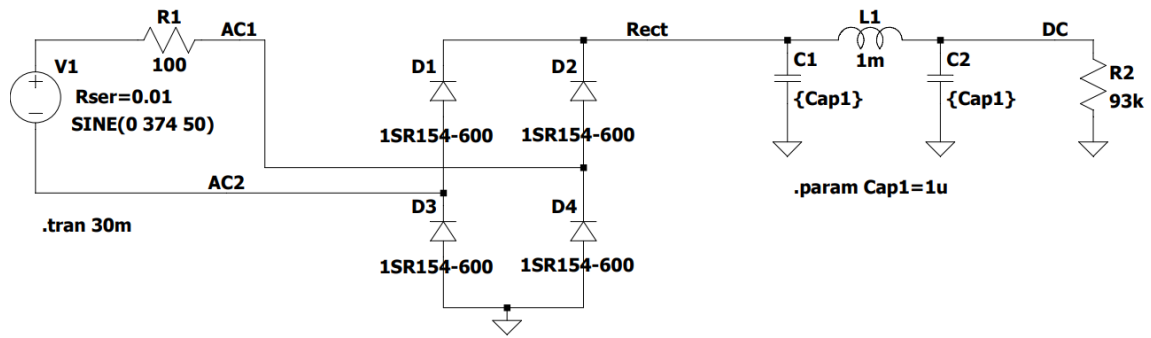


Figure 4.6 LTspice circuit used to simulate inrush current

Considering the maximum specified output power requirement of 1 W while assuming an EVB equivalent converter efficiency of about 65% at the rated load, the corresponding input power is approximately 1,5 W. To simulate this condition, the load resistor R2 (Figure 4.6) value is set to 93 k Ω . Setting the inrush current limiting resistor R1 value to 100 Ω , limits the peak inrush current to a maximum value of 230 mA. Although the peak input power reaches a maximum value of 5,15 W, the pulse is momentary, with a total energy of less than 15 mJ. This value is far below the selected resistor's pulse withstand capability of 3,5 J. Simulation results depicting the inrush current, power loss on the inrush current limiting resistor, and the power loss on the load resistor R2 are depicted below (Figure 4.7).

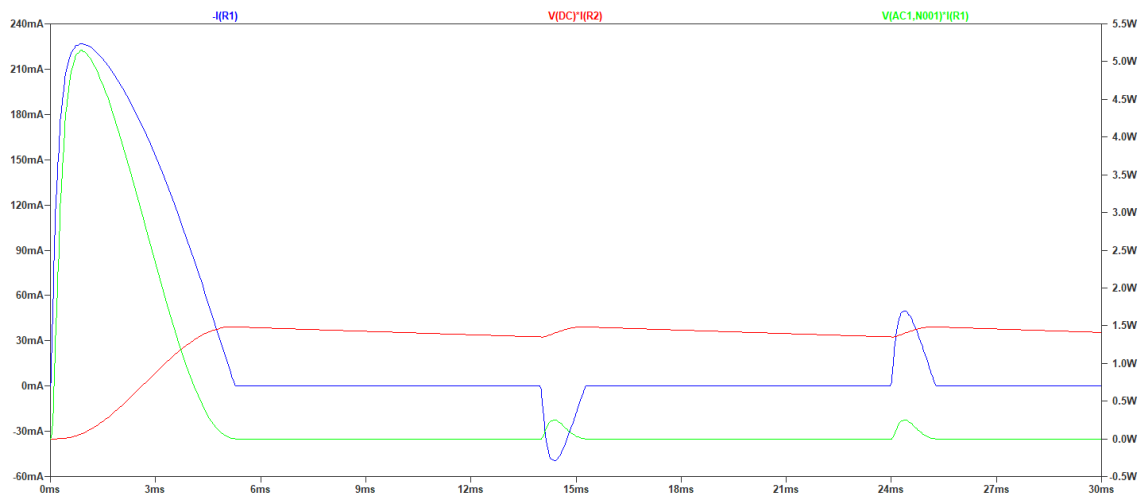


Figure 4.7 LTspice simulation results depicting inrush current - blue line, $-I(R1)$; power loss on the ICL - green line, $V(AC1, N001)*I(R1)$; power loss on the load resistor - red line, $V(DC)*I(R2)$

Next, to determine the average power losses caused by the ICL during normal operating conditions, the input current first needs to be determined:

$$P_{out} = P_{in} \cdot \varepsilon_{flyback} = V_{in} \cdot I_{in} \cdot \varepsilon_{flyback} \Rightarrow I_{in} = \frac{P_{out}}{V_{in} \cdot \varepsilon_{flyback}}, \quad (4.3)$$

where V_{in} - RMS value of the AC mains voltage, V,

P_{in} - input power, W,

P_{out} - output power, W,

I_{in} - input current, A,

$\varepsilon_{flyback}$ - efficiency of the power converter.

Substituting the estimated efficiency of 65% at a 1 W load, and the RMS mains voltage of 230 V into equation 4.3, the maximum RMS value of the input current is calculated:

$$I_{in} = \frac{1 \text{ W}}{230 \text{ V} \cdot 0,65} \approx 6,7 \text{ mA}.$$

The power loss caused by the ICL can now be determined:

$$P_{ICL} = I_{in}^2 \cdot R_{ICL} \quad (4.4)$$

where P_{ICL} - power loss caused by the ICL's resistance, W,

R_{ICL} -resistance of the ICL, Ω .

Substituting the nominal ICL resistance of 100 Ω and the calculated input current values into equation 4.4 provides the maximum power loss value:

$$P_{ICL} = (6,7 \text{ mA})^2 \cdot 100 \Omega \approx 4,5 \text{ mW}.$$

Given that the device normally operates at a much lower power consumption, it is apparent that the power loss caused by the ICL can be considered insignificant.

The metal oxide varistor, RV1 is used to clamp the AC mains voltage in case of line surge events. The failure mode of a varistor is a short circuit. Therefore, when an overvoltage or input short circuit condition occurs, the fusible resistor will fuse silently after overload power is maintained for the specified fusing time. Consequently, either event will cause the subsequent system elements to become disconnected from mains voltage to avoid being damaged.

An 800 V rated bridge rectifier provides full-wave rectification of the input signal. This is followed by an LC filter used for EMI suppression. For this design, the values of the filter components were referenced from the converter's EVB circuit design, as no electromagnetic compatibility pre-compliance test data is available for the first prototype. Subsequent testing will provide information on the changes that need to be made in the input filter design. The second electrolytic capacitor C12 provides a smoother rectified input voltage signal on the V_{BULK} node entering the primary winding.

Connected to the drain node is a snubber circuit comprising a resistor, a capacitor, and a diode designated on the schematic as R2, C3, and D2 respectively. The purpose of this circuit is to suppress the excessive voltage caused by the resonance between the transformer's leakage inductance and the switching MOSFET's parasitic capacitance. Without reference to previous designs, the initial estimate values of snubber components can be determined with the following calculations. The value of the snubber resistor can be estimated as follows [69]:

$$R_{sn} = \frac{V_{sn}^2}{\frac{1}{2} L_{lk} I_{peak}^2 \frac{V_{sn}}{V_{sn} - nV_{out}} f_s}, \quad (4.5)$$

where R_{sn} - snubber resistor's resistance, Ω ,

V_{sn} - voltage across the capacitor, V,

L_{lk} - leakage inductance of the flyback transformer's primary winding, H,

V_{out} - output voltage from the secondary winding, V,

f_s - is the MOSFET switching frequency, Hz,

I_{peak} - is the peak primary current, A,

n - turns ratio between the primary and secondary windings.

The voltage V_{sn} across the snubber capacitor added to the input voltage determines the maximum voltage stress on the switch. This value should be determined at the minimum input voltage and full-load conditions. Generally, it should be set to a value approximately 2 to 2,5 times greater than the value of the voltage reflected from the secondary $n \cdot V_{out}$. Setting the voltage across the capacitor to a small value is unfavorable, as this will result in significant losses in the snubber circuit. [69]

Considering the notable amount of power that can be emitted by the snubber circuit, the power rating of the snubber resistor is important. The power emitted by the snubber resistor can be calculated as follows [69]:

$$P = \frac{V_{sn}^2}{R_{sn}}, \quad (4.6)$$

where P - value of the power emitted by the snubber resistor, W.

Next, the value of the snubber capacitor can be determined [69]:

$$C_{sn} = \frac{V_{sn}}{\Delta V_{sn} R_{sn} f_s}, \quad (4.7)$$

where ΔV_{sn} - maximum ripple of the snubber capacitor voltage, V.

The ripple value is set by the designer and in general, a value between 5% to 10% of the voltage across the snubber capacitor is considered reasonable. The following table depicts calculations for the power supply operated at full load given relevant values from components' datasheets (Table 4.5). [69]

Table 4.5 Calculation of snubber component values

Parameters	Value	Unit	Comment
V_{sn}	170	V	2 times the voltage reflected from secondary
L_{lk}	20	μH	WE 750871013 transformer's typical leakage inductance value
I_{peak}	350	mA	VIPER06 converter's typical drain current limit value
n	17:1	turns	Transformer's nominal turns ratio between primary and secondary windings
V_{out}	5	V	Nominal output voltage
f_s	60	kHz	Nominal switching frequency of the converter
ΔV_{sn}	$0,1V_{sn}$	V	Maximum ripple of the capacitor voltage is selected to be 10% of the snubber voltage
Calculated values	Value	Unit	Comment
R_{sn}	197	k Ω	Calculated using equation 4.5
C_{sn}	848	pF	Calculated using equation 4.7
P	0,147	W	Calculated using equation 4.6

During the initial EVB testing, it was observed that under the tested load conditions, the drain node peak-to-peak voltage remained well under the switch specified limit of 800 V, not exceeding 500 V at any point. Therefore, the initial values of the snubber components were referenced from the EVB design. Furthermore, the calculated values

depicted in Table 4.5 are relatively close to the values used on the EVB. If during power supply prototype testing it is observed that the maximum voltage stress on the MOSFET exceeds 80% of its rated voltage, then the snubber will have to be redesigned by selecting different resistance and capacitance values.

To protect the flyback controller's supply voltage pin, a Zener diode with a series current limiting resistor is used. The reverse breakdown voltage or equivalently, Zener voltage of the selected component is 18 V. This is higher than the transformer's specified auxiliary winding output voltage of 15 V, while not exceeding the controller's maximum supply voltage value of 23,5 V. Selecting a Zener diode that starts to clamp the voltage too close to the nominal auxiliary winding output, will cause additional losses as the component will be continuously conducting notable current. Additionally, a 10 μ F electrolytic capacitor is placed on the supply pin, which supplies the IC after the MOSFET starts switching.

Resistor R12 connected to the LIM pin of the controller can be used to limit the value of the drain current. The maximum drain current limit value of 0,38 A specified in the converter's datasheet is greater than the transformers listed saturation current of 0,35 A. At this point, the primary inductance has already decreased by approximately 20% from the initial typical value of 1,8 mH. However, due to the low power consumption of the device during normal operation, the power supply should always remain in burst mode. The drain current in this mode is typically limited to only 85 mA and consequently, a current limiting resistor is not required in this application.

Since the power converter utilizes secondary side regulation, the converter's feedback FB pin must be shorted to ground to disable the internal error amplifier. Instead, the converter's COMP pin is used to connect to an internal voltage reference. Externally, the COMP pin is connected to a loop compensation network comprising capacitors C18, and C21, as well as resistor R13. Components R11 and C17 on the secondary side are also used for compensation. Their initial values are referenced from the EVB's circuit design, as the EVB output remained stable during load tests. Should this not be the case for the prototype, the compensation component values will be adjusted based on frequency response measurements.

To receive feedback from the secondary, an optocoupler is used to cross the isolation barrier, while maintaining galvanic isolation. Therefore, the optocoupler was selected with a sufficient isolation test voltage rating of 5,3 kV. Connected to the optocoupler's

cathode, is an adjustable voltage reference designated as U4 on the schematic. This is used to set the secondary output voltage level by selecting the voltage divider resistor values R8 and R14 correspondingly. Resistor R7 is used to bias the light-emitting diode of the optocoupler, while resistor R19 provides a minimum biasing current to the adjustable voltage reference U4. [70]

4.6 Power supply prototype testing

The power supply prototype was initially tested under different loads, ranging from a no-load condition to the maximum specified output power of 1 W. It should be noted that during these tests, only the 5 V output was loaded. As the LDO is always enabled while the converter is powered, its small quiescent current adds an additional loss factor. This additional power loss should mostly be negligible, however, as the LDO's datasheet [71] specifies a typical no-load quiescent current of 50 μA , resulting in power consumption of well under 1 mW. Parameters considered during testing were the power supply output load regulation, output ripple voltage, efficiency, and power loss. The output voltage values were recorded at every tested load point to determine how closely the converter maintains the set output voltage of 5 V (Figure 4.8).

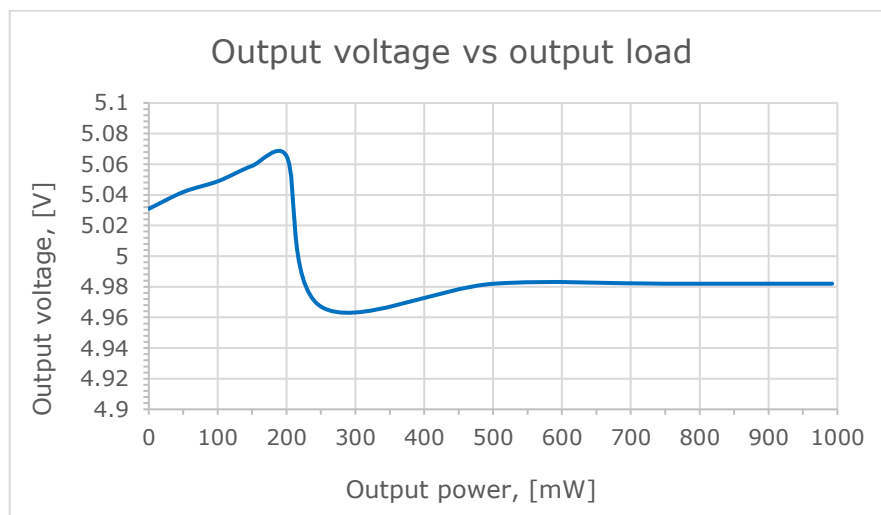
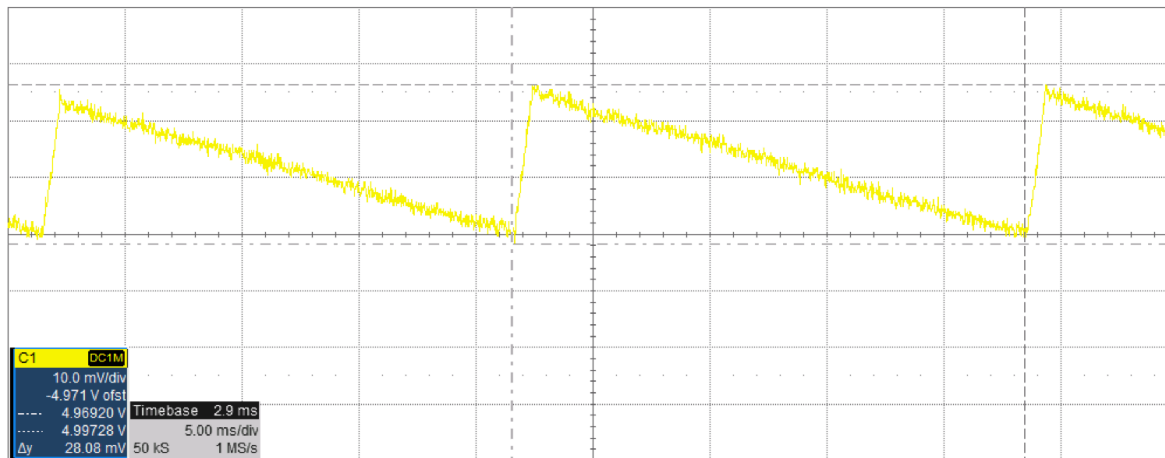


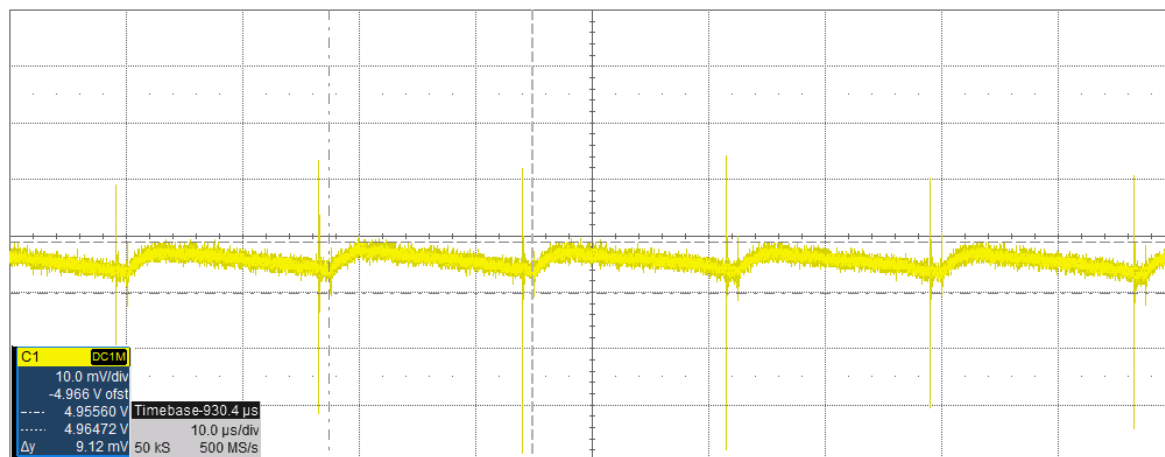
Figure 4.8 Output voltage regulation under different load conditions

At very light loads, the converter operates deep in burst-mode which results in cycles of multiple bursts with a frequency of tens to a few hundred hertz between consecutive cycles. Thus, the output voltage slightly exceeds the set value in no-load and light-load conditions. Nevertheless, the output voltage stays within an acceptable 1,5% of the

specified value of 5 V over the entire tested range. The output voltage ripple in no-load and maximum specified load conditions is depicted below (Figure 4.9).



a) Output voltage ripple in no-load



b) Output voltage ripple at a load of 1 W

Figure 4.9 Output voltage ripple in a) no-load conditions, and b) at a load of 1 W

As previously mentioned, the unloaded voltage ripple of the 5 V output must remain within 30 mV peak to peak to meet the specifications of the environmental sensor it supplies. These results indicate that the selected output filter component values are sufficient; however, additional ceramic capacitors with low equivalent series resistance can be added to the output to decrease the ripple further.

Similar to the EVB load tests, the power loss and converter efficiency values were recorded as the 5 V output was loaded (Figure 4.10).

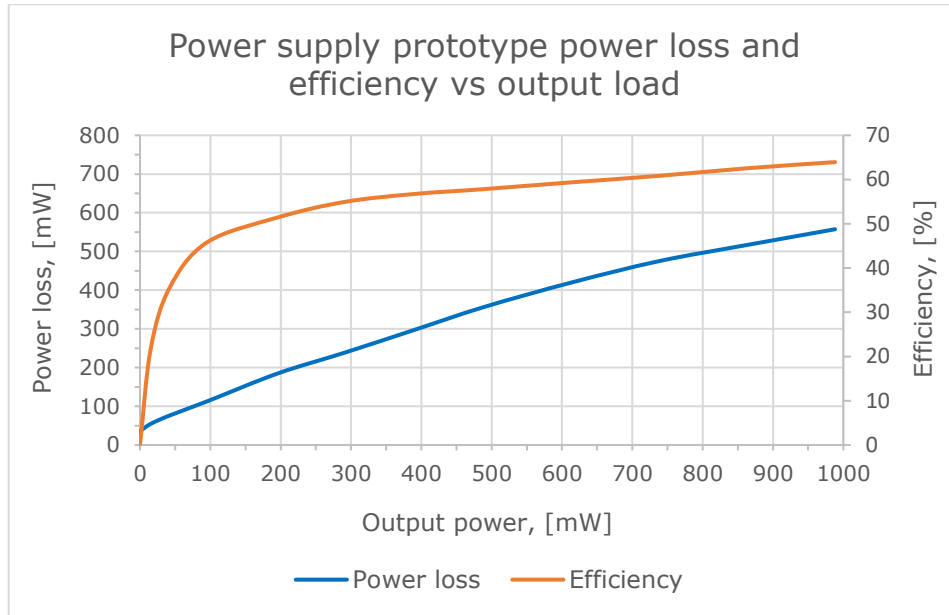


Figure 4.10 Power loss and efficiency values of the power supply prototype under different load conditions

Although the results obtained with the power supply prototype provided no improvement over the tested EVB, the light-load power loss values remain within the acceptable limit previously determined. The graph above does not include the additional power loss caused by the LDO, which must also be considered. The average typical power consumption of the device includes the consumption of components supplied from both 5 V and 3,3 V. However, the worst-case power loss where all devices are powered by 3,3 V, can be estimated as follows:

$$P_{LDO} = \frac{P_{typ} \cdot (V_{flyback} - V_{LDO})}{V_{LDO}} + I_{supply} \cdot V_{LDO}, \quad (4.8)$$

where P_{LDO} – worst-case additional power loss caused by the LDO, W,

P_{typ} – average power consumption during typical operation, W

$V_{flyback}$ – nominal output voltage of the flyback, V,

V_{LDO} – nominal output voltage of the LDO, V,

I_{supply} – typical specified supply current to the LDO during operation at 20 mW load, A.

Substituting each parameter value into equation 4.8, provides the following result:

$$P_{LDO} = \frac{0,02 \text{ W} \cdot (5 \text{ V} - 3,3 \text{ V})}{3,3 \text{ V}} + 0,7 \cdot 10^{-4} \text{ A} \cdot 3,3 \text{ V} \approx 10,5 \text{ mW}$$

It is evident that adding the obtained value to the recorded converter power loss at a 20 mW output load will not cause the total losses to exceed 75 mW. Nonetheless, the overall efficiency of the converter is relatively poor over the whole specified range. Observing the power supply with a thermal camera indicates that the two primary sources of power loss are the controller IC and the transformer. While optimizing the selected component values and finding a more efficient controller IC can provide improvements, the effect is likely marginal in such low output power application. Moreover, the available selection of off the shelf flyback transformers viable for this application is very limited. To considerably reduce the losses caused by the transformer, a custom component would have to be designed and optimized. However, this would significantly increase design related costs and the design time. Therefore, it is likely that the isolated flyback topology is not the best option to achieve good efficiency at very light loads. An alternative option to consider for the next prototype is to use a non-isolated power supply, e.g., an offline buck converter. The safety isolation could then instead be achieved with the device's enclosure design. If this is achieved, using an offline buck converter would solve the primary design related concerns. First, the available space allocated for the power supply is not an issue, as the topology does not require a bulky transformer and has an overall lower component count. Second, it is possible to achieve significantly higher efficiencies at the typical operating power of this device, reducing power lost as heat.

SUMMARY

Indoor air quality is a topic of great importance, as the majority of the population spend up to 90% of their day indoors. This accentuates the fact that poor indoor air quality has been found to be a cause of various adverse health effects. Consequently, monitoring of indoor air quality parameters in commonly occupied spaces is necessary to determine if the present conditions are adequate. In the conducted literature review, it was found that most of the previously developed solutions are either battery powered or require an external power supply. However, battery powered devices are inconvenient in many applications, as they require changing or recharging of the batteries periodically. Although devices with external power supplies do not need additional attention, cables connecting the devices to their power supply require cable management on the part of the user and are generally undesired from an aesthetic perspective.

The current thesis work aims to develop integral parts of a device that neither requires periodical attention nor any cable management from the user. This indoor air quality monitoring device is wireless, mains powered and can be installed inside a common junction box to maintain visual appeal. The device comprises two main parts, a sensor board, and a power supply, which are assembled using pin headers to establish both a mechanical and electrical connection. The sensor board contains a radio module for wireless communications, as well as several indoor air quality sensors to record key environmental and air quality parameters such as concentrations of carbon dioxide and total volatile organic compounds, temperature, and relative humidity. The power supply converts mains voltage into a low voltage direct current signal to supply the sensor board components. Due to the limited space inside a junction box, the size restrictions were a primary consideration for both component selection and design of the boards.

As a result of this thesis work, a viable chip antenna was selected, and an accompanying circuit was designed for the radio module. A selection of chip antennas was first gathered which were subjected to preliminary testing using a vector network analyzer. Observing the return loss parameter of each considered antenna on the sensor board provided sufficient information to select a viable model for the final design. This antenna was subsequently tested on the finalized radio module to verify its performance. Comparative tests including received signal amplitude measurements with a spectrum analyzer and a measurement antenna were conducted to obtain relative radiation patterns. The performance of the radio module was then compared to the reference

device provided by the customer company. The latter is a device that has been tested in real applications and has proven to work adequately. The results of the comparative tests indicated that the new radio module generally outperformed the reference device and did not perform considerably worse in any of the tested configurations. Nevertheless, further testing should be conducted to determine the absolute gain of the new radio module's antenna, as well as the maximum range of reception in outdoor conditions with minimal interference.

A prototype of the power supply was designed in isolated flyback topology considering its relative simplicity and small component count compared to other applicable isolated switched mode power supply topologies. As the device is connected directly to mains, it was specified that the low voltage output must be isolated from the input. Therefore, relevant safety standards were referenced to establish the applicable clearance and creepage distances on the power supply printed circuit board. Additionally, the flyback transformer was selected with a sufficient insulation voltage rating between its primary and secondary windings. Initial converter and transformer testing was done on an evaluation board of the selected flyback controller chip. Comparative tests were conducted considering the power supply efficiency and power losses to determine a viable transformer option. Power loss of the converter is a key parameter to consider, as generation of excess heat will interfere with the operation of the sensors. A setup of the device's typical installation configuration was constructed to estimate the temperature increase inside the junction box during the device's typical operation. Considering the evaluation board's power loss values as a reference, it was concluded that the converter is adequate in the current application. Subsequently, the evaluation board was referenced for the current power supply prototype design.

The power supply design provided no further improvement compared to the evaluation board. Furthermore, while the power loss values remained within the acceptable limits, the overall efficiency of the converter is relatively poor. The results suggest that the chosen topology is suboptimal, and a more efficient non-isolated power supply, e.g., an offline buck converter should be designed instead. Ensuring safety isolation could then be achieved by the design of an enclosure for the device. Moreover, this solution would address the primary design concern of limited space availability.

KOKKUVÕTE

Siseõhu kvaliteet omab inimesele olulist mõju arvestades, et tänapäeval veedab enamik populatsioonist kuni 90% oma ajast siseruumides. Siseõhukvaliteedi olulisuse toob eriti välja asjaolu, et õhusaaste võib avaldada tervisele tõsist negatiivset mõju. Seetõttu on peamiste siseõhukvaliteedi parameetrite jälgimine sagedasti kasutatavates ruumides märkimisväärse tähtsusega. Kirjanduse ülevaates uuritud siseõhukvaliteedi jälgimislahendustest kasutavad enamik patareid - ja akutoide või välist toiteallikat. Patareid - ja akutoitel põhinevad seadmed vajavad aga aeg-ajalt kasutajapoolset patareid vahetamist või akude laadimist. Väliste toiteallikaga seadme puhul seevastu kaasnevad seadmega tihti tüliliks osutuvad ühendusjuhtmed, mis ei ole soovitatavad mitte ainult praktilisest, kuid ka esteetilisest vaatenurgast.

Käesolev lõputöö käsitleb võrgutoitel raadioliidesega siseõhu kvaliteedi mõõteseadme oluliste osade väljatöötlust ja arendust. See seade on mõeldud paigaldamiseks harutoosi, mis läbi on võimalik vältida eelnimetatud probleeme, mis kaasnevad aku - ja patareidtoitel põhinevate ning väliste toiteallikaga seadmetega. Antud seade koosneb kahest peamisest osast, andurplaadist koos raadiomooduli ja erinevaid siseõhukvaliteedi parameetreid jälgivate anduritega ning toiteploki, mis muundab võrgupinge andurplaadi komponentidele sobivaks madalapingeliseks alalisvooluks. Seadmele seab ranged füüsilised piirangud asjaolu, et see peab mahtuma harutoosi. Sellest tulenevaid piiranguid on kõigi seadmeosade arendusel ka arvesse võetud.

Käesoleva töö tulemusena valiti esmalt välja rakendusse sobiv antenn ning disainiti väljavalitud antennile vastav toiteahel. Antenni esmasel valikul lähtuti erinevate antennimudelite S11 parameetrist, mis määrati võrguanalüsaatoriga. Valmis raadiomoodulit väljavalitud antenniga võrreldi ka kliendifirma referents-seadmega, mille töötamine reaalsetes tingimustes on varasemal katsetamisel kindlaks tehtud. Võrdluse loomiseks leiti spektrianalüsaatori abil testitavate seadmete suhtelised suunadiagrammid. Katsetulemustest järeldus, et uus raadiomoodul toimib enamikes katsetatud asetustes paremini või vähemalt ligikaudu võrdväärselt võrdlusseadmega. Saadud võrdlevad katsetulemused on küll indikatsioon raadiomooduli sobivusest antud rakenduses, kuid järgnevalt tuleks katsetada raadiomoodulit ka reaalsetes töötingimustes, näiteks leida seadme tegelik edastuskaugus viies see sobivatesse välistingimustesse, kus puudusid katsetamist häirivad signaalid.

Seadme toiteploki esmane prototüüp disainiti toiteploki isoleeritud „flyback” topoloogias, arvestades selle suhtelist lihtsust ja realiseerimiseks vajaminevate komponentide vähest arvu. Kuna seade ühendatakse otse võrgupingele, oli seadme arendusel ettenähtud ka sisend – ja väljundahela vahel piisava isolatsiooni tagamine. Seetõttu võeti toiteploki disainil arvesse ka asjakohastes ohutusstandardites sätestatud nõudeid nagu näiteks minimaalne lubatud roomamistee ning kasutatava trafo primaar - ja sekundaarpoole vaheline minimaalne lubatud isolatsioonitugevus. Esmased pingemuunduri ja trafo katsed teostati valitud “flyback” kontrolleri vastaval arendusplaadil. Vastavalt peamistele valikukriteeriumitele, milleks olid muunduri võimsuskadud ja efektiivsus, valiti katsetulemuste põhjal välja sobiv trafomudel. Võimsuskadudest tuleneva temperatuuritõusu hindamiseks harutoosis, konstrueeriti reaalseid tingimusi jäljendav testsein. Kasutades arendusplaadi katsetest leitud keskmisi võimsuskadusid, sai järeldada, et temperatuuri tõus harutoosis jääb aktsepteeritavatesse piiridesse ning valitud muunduri arendusplaadi võib võtta aluseks toiteploki prototüübi disainil.

Prototüübi katsetest selgus, et kuigi saavutatud võimsuskadud püsisid seatud piirides, on muunduri üldine efektiivsus siiski suhteliselt madal. Tulemustest võib järeldada, et valitud toiteploki topoloogia ei ole antud lahenduse jaoks kõige optimaalsem. Tõenäoliselt saavutaks madalal võimsusel töötades oluliselt parema efektiivuse ja madalamad võimsuskadud kasutades isoleerimata pingemuundurit, näiteks võrgupingel töötavat „buck” muundurit. Sellisel juhul tuleks ohutisolatsioon tagada seadme kesta disaini abil. Arvestades sellise topoloogia suuremat lihtsust ja vähemat komponentide arvu, aitaks selline lahendus tõenäoliselt lisaks väiksemate võimsuskadude saavutamisele vältida ka enamikke disainipiiranguid, mis tulenevad piiratud ruumist harutoosis.

LIST OF REFERENCES

- [1] United Nations Environment Programme. "In historic move, UN declares healthy environment a human right." [unep.org](https://www.unep.org/news-and-stories/story/historic-move-un-declares-healthy-environment-human-right). Accessed: Dec. 13, 2023. [Online]. Available: <https://www.unep.org/news-and-stories/story/historic-move-un-declares-healthy-environment-human-right>
- [2] N. Mahyuddin and H.B. Awbi, "A Review of CO₂ Measurement Procedures in Ventilation Research," *Int. J. Vent.*, vol. 10, no. 4, pp. 353–370, Mar. 2012, doi: 10.1080/14733315.2012.11683961.
- [3] World Health Organization, "WHO global air quality guidelines: particulate matter (PM_{2.5} and PM₁₀), ozone, nitrogen dioxide, sulfur dioxide and carbon monoxide," 2021. Accessed: Dec. 13, 2023. [Online]. Available: <https://www.who.int/publications-detail-redirect/9789240034228>
- [4] uHoo. *uHoo Smart Air Monitor User Manual*. Accessed: Apr 19, 2024. [Online]. Available: https://getuhoo.com/wp-content/themes/new-woocommerce-theme/assets/pdf/uHoo_Smart_Air_Monitor_User_Manual.pdf
- [5] Qingping. "Qingping Air Monitor - Specifications." [qingping.co](https://www.qingping.co/air-monitor/specifications). Accessed: Apr. 27, 2024. [Online]. Available: <https://www.qingping.co/air-monitor/specifications>
- [6] AirGradient. "AirGradient ONE - Award Winning Indoor Monitor." [airgradient.com](https://www.airgradient.com/indoor/). Accessed: Apr. 27, 2024. [Online]. Available: <https://www.airgradient.com/indoor/>
- [7] IKEA. "VINDSTYRKA." [ikea.com](https://www.ikea.com/gb/en/manuals/vindstyrka-air-quality-sensor-smart__AA-2351596-1-100.pdf). Accessed: Apr. 19, 2024. [Online]. Available: https://www.ikea.com/gb/en/manuals/vindstyrka-air-quality-sensor-smart__AA-2351596-1-100.pdf
- [8] Airthings. "View Plus." [airthings.com](https://www.airthings.com/en/view-plus). Accessed: Apr. 27, 2024. [Online]. Available: <https://www.airthings.com/en/view-plus>
- [9] Aranet, "Aranet4 HOME." [aranet.com](https://cdn.bfldr.com/FS48XT6B/at/k9b9wjnv8f455crkp7846j/Aranet4_datasheet_v25_WEB.pdf). Accessed: Apr. 19, 2024. [Online]. Available: https://cdn.bfldr.com/FS48XT6B/at/k9b9wjnv8f455crkp7846j/Aranet4_datasheet_v25_WEB.pdf
- [10] .AirQM. "Awair Element." [dotairqm.com](https://dotairqm.com/pages/specifications). Accessed: Apr. 27, 2024. [Online]. Available: <https://dotairqm.com/pages/specifications>
- [11] INKBIRD. "IAM-T1." [inkbird.com](https://inkbird.com/cdn/shop/files/English_User_Manual_for_Air_Quality_Monitor_IAM-T1.pdf?v=14889863157034407635). Accessed: Apr. 19, 2024. [Online]. Available: https://inkbird.com/cdn/shop/files/English_User_Manual_for_Air_Quality_Monitor_IAM-T1.pdf?v=14889863157034407635

- [12] Temtop. "Air Station User Manual P100/M100." Accessed: Apr. 27, 2024. [Online]. Available: <https://drive.google.com/file/d/17R-GXetOe1iHbBaqXpaJO38RsrUX6RRO/view>
- [13] Amazon. "Amazon Smart Air Quality Monitor – Know your air, Works with Alexa." amazon.com. Accessed: Apr. 27, 2024. [Online]. Available: <https://www.amazon.com/Introducing-Amazon-Smart-Quality-Monitor/dp/B08W8KS8D3?th=1>
- [14] IQAir. "IQAir AirVisual Pro." iqair.com. Accessed: Apr. 27, 2024. [Online]. Available: <https://www.iqair.com/products/air-quality-monitors/airvisual-pro-indoor-monitor>
- [15] Kaiterra. "Technical Specifications (SE-100)." Accessed: Apr. 19, 2024. [Online]. Available: [https://3782315.fs1.hubspotusercontent-na1.net/hubfs/3782315/Marketing%20Collateral/Technical%20Specifications/Sensedge%20Technical%20Specifications%20\(2024\).pdf?_hstc=204925903.7f6d697601cfb0458d1649f1722fb611.1713378571462.1713378571462.1713378571462.1&__hssc=204925903.1.1713378571462&__hsfp=191606704&hsCtaTracking=919ed0a5-6b48-4173-b06f-d1c834ac92e4%7C6191313a-2cbd-44df-af19-5fdc9c1c6bc2](https://3782315.fs1.hubspotusercontent-na1.net/hubfs/3782315/Marketing%20Collateral/Technical%20Specifications/Sensedge%20Technical%20Specifications%20(2024).pdf?_hstc=204925903.7f6d697601cfb0458d1649f1722fb611.1713378571462.1713378571462.1713378571462.1&__hssc=204925903.1.1713378571462&__hsfp=191606704&hsCtaTracking=919ed0a5-6b48-4173-b06f-d1c834ac92e4%7C6191313a-2cbd-44df-af19-5fdc9c1c6bc2)
- [16] ATMO. "Atmotube Technical Specifications." atmotube.com. Accessed: Apr. 27, 2024. [Online]. Available: <https://atmotube.com/atmotube-support/atmotube-technical-specification>
- [17] J. Saini, M. Dutta, and G. Marques, "Indoor Air Quality Monitoring Systems Based on Internet of Things: A Systematic Review," *Int. J. Environ. Res. Public Health*, vol. 17, no. 14, Art. no. 4942, Jul. 2020, doi: 10.3390/ijerph17144942.
- [18] J. Saini, M. Dutta, and G. Marques, "A comprehensive review on indoor air quality monitoring systems for enhanced public health," *Sustain. Environ. Res.*, vol. 30, Art. no. 6, Jan. 2020, doi: 10.1186/s42834-020-0047-y.
- [19] M. Benammar, A. Abdaoui, S. H. M. Ahmad, F. Touati, and A. Kadri, "A Modular IoT Platform for Real-Time Indoor Air Quality Monitoring," *Sensors*, vol. 18, no. 2, Art. no. 581, Feb. 2018, doi: 10.3390/s18020581.
- [20] G. Marques, C. Roque Ferreira, and R. Pitarma, "A System Based on the Internet of Things for Real-Time Particle Monitoring in Buildings," *Int. J. Environ. Res. Public Health*, vol. 15, no. 4, Art. no. 821, Apr. 2018, doi: 10.3390/ijerph15040821.
- [21] X. Yang, L. Yang, and J. Zhang, "A WiFi-enabled indoor air quality monitoring and control system: The design and control experiments," in *2017 13th IEEE International Conference on Control & Automation (ICCA)*, Jul. 2017, pp. 927–932. doi: 10.1109/ICCA.2017.8003185.

- [22] G. Marques and R. Pitarma, "An Internet of Things-Based Environmental Quality Management System to Supervise the Indoor Laboratory Conditions," *Appl. Sci.*, vol. 9, no. 3, Art.no. 438, Jan. 2019, doi: 10.3390/app9030438.
- [23] F. Salamone, L. Belussi, L. Danza, T. Galanos, M. Ghellere, and I. Meroni, "Design and Development of a Nearable Wireless System to Control Indoor Air Quality and Indoor Lighting Quality," *Sensors*, vol. 17, no. 5, Art. no. 1021. May 2017, doi: 10.3390/s17051021.
- [24] N. Azmi et al., "Design and Development of Multi-Transceiver Lorafi Board consisting LoRa and ESP8266-Wifi Communication Module," *IOP Conf. Ser. Mater. Sci. Eng.*, vol. 318, Art. no. 012051, Mar. 2018, doi: 10.1088/1757-899X/318/1/012051.
- [25] F. Salamone, L. Belussi, L. Danza, M. Ghellere, and I. Meroni, "Design and Development of nEMoS, an All-in-One, Low-Cost, Web-Connected and 3D-Printed Device for Environmental Analysis," *Sensors*, vol. 15, no. 6, Art. no. 13012-13027, Jun. 2015, doi: 10.3390/s150613012.
- [26] L. Zhao, W. Wu, and S. Li, "Design and Implementation of an IoT-Based Indoor Air Quality Detector With Multiple Communication Interfaces," *IEEE Internet of Things J.*, vol. 6, no. 6, pp. 9621–9632, Jul. 2019, doi: 10.1109/JIOT.2019.2930191.
- [27] Z. Tu, C. Hong, and H. Feng, "EMACS: Design and implementation of indoor environment monitoring and control system," in *2017 IEEE/ACIS 16th International Conference on Computer and Information Science (ICIS)*, May 2017, pp. 305–309. doi: 10.1109/ICIS.2017.7960010.
- [28] M. Taştan and H. Gökozan, "Real-Time Monitoring of Indoor Air Quality with Internet of Things-Based E-Nose," *Appl. Sci.*, vol. 9, no. 16, Art. no. 3435, Jan. 2019, doi: 10.3390/app9163435.
- [29] N. Zakaria, Z. Zainal Abidin, N. Harum, L. Hau, N. Ali, and F. Jafar, "Wireless Internet of Things-Based Air Quality Device for Smart Pollution Monitoring," *Int. J. Adv. Comput. Sci. Appl.*, vol. 9, no. 11, pp. 65–69, Nov. 2018, doi: 10.14569/IJACSA.2018.091110.
- [30] A. Martín-Garín, J. A. Millán-García, A. Baïri, J. Millán-Medel, and J. M. Salazar-Lizarraga, "Environmental monitoring system based on an Open Source Platform and the Internet of Things for a building energy retrofit," *Autom. Constr.*, vol. 87, pp. 201–214, Mar. 2018, doi: 10.1016/j.autcon.2017.12.017.
- [31] J. Velicka, M. Pies, and R. Hajovsky, "Wireless Measurement of Carbon Dioxide by use of IQRF Technology," *IFAC-Pap.*, vol. 51, no. 6, pp. 78–83, Jan. 2018, doi: 10.1016/j.ifacol.2018.07.133.

- [32] J. Kang and K.-I. Hwang, "A Comprehensive Real-Time Indoor Air-Quality Level Indicator," *Sustainability*, vol. 8, no. 9, Art. no. 881, Sep. 2016, doi: 10.3390/su8090881.
- [33] G. Marques and R. Pitarma, "A Cost-Effective Air Quality Supervision Solution for Enhanced Living Environments through the Internet of Things," *Electronics*, vol. 8, no. 2, Art. no. 170, Feb. 2019, doi: 10.3390/electronics8020170.
- [34] G. Marques, I. M. Pires, N. Miranda, and R. Pitarma, "Air Quality Monitoring Using Assistive Robots for Ambient Assisted Living and Enhanced Living Environments through Internet of Things," *Electronics*, vol. 8, no. 12, Art. no. 1375, Nov. 2019, doi: 10.3390/electronics8121375.
- [35] M. Rahman et al., "An adaptive IoT platform on budgeted 3G data plans," *J. Syst. Archit.*, vol. 97, pp. 65–76, Aug. 2019, doi: 10.1016/j.sysarc.2018.11.002.
- [36] M. Karami, G. V. McMorrow, and L. Wang, "Continuous monitoring of indoor environmental quality using an Arduino-based data acquisition system," *J. Build. Eng.*, vol. 19, pp. 412–419, Sep. 2018, doi: 10.1016/j.job.2018.05.014.
- [37] G. Marques, N. Miranda, A. Kumar Bhoi, B. Garcia-Zapirain, S. Hamrioui, and I. de la Torre Díez, "Internet of Things and Enhanced Living Environments: Measuring and Mapping Air Quality Using Cyber-physical Systems and Mobile Computing Technologies," *Sensors*, vol. 20, no. 3, Art. no. 720, Jan. 2020, doi: 10.3390/s20030720.
- [38] S. Girish, P. Rajiah, and A. Ganesh, "Real-Time Remote Monitoring of Indoor Air Quality Using Internet of Things (IoT) and GSM Connectivity," in *ICAIECES 2015*, 2016, pp. 527–533. doi: 10.1007/978-81-322-2656-7_48.
- [39] Q. Ha, S. Metia, and M. D. Phung, "Sensing Data Fusion for Enhanced Indoor Air Quality Monitoring," *IEEE Sens. J.*, vol. 20, pp. 4430–4441, Mar. 2020, doi: 10.1109/JSEN.2020.2964396.
- [40] G. Marques and R. Pitarma, "An Indoor Monitoring System for Ambient Assisted Living Based on Internet of Things Architecture," *Int. J. Environ. Res. Public Health*, vol. 13, no. 11, Art. no. 1152, Nov. 2016, doi: 10.3390/ijerph13111152.
- [41] Z. Idrees, Z. Zou, and L. Zheng, "Edge Computing Based IoT Architecture for Low Cost Air Pollution Monitoring Systems: A Comprehensive System Analysis, Design Considerations & Development," *Sensors*, vol. 18, no. 9, Art. no. 3021, Sep. 2018, doi: 10.3390/s18093021.
- [42] G. D. Moiş, T. Sanislav, S. C. Folea, and S. Zeadally, "Performance Evaluation of Energy-Autonomous Sensors Using Power-Harvesting Beacons for Environmental Monitoring in Internet of Things (IoT)," *Sensors*, vol. 18, no. 6, Art. no. 1709, Jun. 2018, doi: 10.3390/s18061709.

- [43] T. Alhmiedat and G. Samara, "A Low Cost ZigBee Sensor Network Architecture for Indoor Air Quality Monitoring," *Int. J. Comput. Sci. Inf. Secur.*, vol. 15, pp. 140–144, Dec. 2017. [Online]. Available: https://www.researchgate.net/publication/316146252_A_Low_Cost_ZigBee_Sensor_Network_Architecture_for_Indoor_Air_Quality_Monitoring
- [44] P. Arroyo, J. L. Herrero, J. I. Suárez, and J. Lozano, "Wireless Sensor Network Combined with Cloud Computing for Air Quality Monitoring," *Sensors*, vol. 19, no. 3, Art. no. 691, Jan. 2019, doi: 10.3390/s19030691.
- [45] T.-C. Yu and C.-C. Lin, "An Intelligent Wireless Sensing and Control System to Improve Indoor Air Quality: Monitoring, Prediction, and Preaction," *Int. J. Distrib. Sens. Netw.*, vol. 2015, no. 8, pp. 1–9, Aug. 2015, doi: 10.1155/2015/140978.
- [46] Bosch Sensortec, "World's smallest PM sensor - BMV080." [bosch-sensortec.com](https://www.bosch-sensortec.com/media/boschsensortec/downloads/product_flyer/bst-bmv080-fl000.pdf). Accessed: Apr. 19, 2024. [Online]. Available: https://www.bosch-sensortec.com/media/boschsensortec/downloads/product_flyer/bst-bmv080-fl000.pdf
- [47] T. Pattnayak and G. Thanikachalam, "Antenna Design and RF Layout Guidelines," Infineon Technologies AG, Neubiberg, Germany. Accessed: Dec. 13, 2023. [Online]. Available: https://www.infineon.com/dgdl/Infineon-AN91445_Antenna_Design_and_RF_Layout_Guidelines-ApplicationNotes-v09_00EN.pdf?fileId=8ac78c8c7cdc391c017d073e054f6227
- [48] M. Reckeweg and C. Rohner, "Antenna Basics," Rohde & Schwarz, Munich, Germany. Accessed: Dec. 13, 2023. [Online]. Available: https://scdn.rohde-schwarz.com/ur/pws/dl_downloads/premiumdownloads/premium_dl_brochures_and_datasheets/premium_dl_whitepaper/Antenna_Basics_8GE01_1e.pdf
- [49] P. Bevelacqua, "Antenna Impedance." [antenna-theory.com](https://www.antenna-theory.com/basics/impedance.php). Accessed: Dec. 14, 2023. [Online]. Available: <https://www.antenna-theory.com/basics/impedance.php>
- [50] Z. Peterson, "S11 Parameter vs. Return Loss vs. Reflection Coefficient: When Are They the Same?" [resources-altium.com](https://resources.altium.com/p/s11-vs-return-loss-vs-reflection-coefficient-when-are-they-same). Accessed: Dec. 14, 2023. [Online]. Available: <https://resources.altium.com/p/s11-vs-return-loss-vs-reflection-coefficient-when-are-they-same>
- [51] M. Kamil, "AN1114 - Switch Mode Power Supply (SMPS) Topologies (Part I)." Microchip Technology Inc., Chandler, AZ, USA. Accessed: Apr. 13, 2024. [Online]. Available: <https://ww1.microchip.com/downloads/en/appnotes/01114a.pdf>
- [52] A. Pini, "Design a Switch Mode Power Supply Using an Isolated Flyback Topology." [digikey.com](https://www.digikey.com/en/articles/design-switch-mode-power-supply-isolated-flyback-topology). Accessed: Dec. 16, 2023. [Online]. Available: <https://www.digikey.com/en/articles/design-switch-mode-power-supply-isolated-flyback-topology>

[53] I. Batarseh and A. Harb, "Isolated Switch-Mode dc-to-dc Converters," in *Power Electronics – Circuit Analysis and Design*, 2nd ed., NYC, NY, USA: Springer Publishing Company, 2018, ch.5, pp. 273–345. Accessed: Apr. 28, 2024. [Online]. Available: <https://link.springer.com/book/10.1007/978-3-319-68366-9>

[54] "How to Keep a FLYBACK Switch Mode Supply Stable with a Critical-Mode Controller," ON Semiconductor Corp., Scottsdale, Arizona, USA. Accessed: Dec. 16, 2023. [Online]. Available: <https://www.onsemi.com/pub/Collateral/AN1681-D.PDF>

[55] T. Hudson, "Primary-Side vs. Secondary-Side Regulation," Monolithic Power Systems Inc., Kirkland, WA, USA. Accessed: Dec. 17, 2023. [Online]. Available: <https://www.monolithicpower.com/en/primary-side-vs-secondary-side-regulation>

[56] *Plugs and socket-outlets for household and similar purposes*, EVS 873:2014, MTÜ Eesti Standardimis- ja Akrediteerimiskeskus, Tallinn, Eesti, Apr. 2014. [Online]. Available: <https://www.evs.ee/en/evs-873-2014>

[57] Q. D. La, D. Nguyen-Nam, M. Ngo, H. Hoang, and T. Quek, "Dense Deployment of BLE-based Body Area Networks: A Coexistence Study," *IEEE Trans. Green Commun. Netw.*, vol. 2, pp. 972–981, Jul. 2018, doi: 10.1109/TGCN.2018.2859350.

[58] *AWR TX-Line*. Cadence. Accessed: Mar. 14, 2023. [Online]. Available: https://www.cadence.com/en_US/home/tools/system-analysis/rf-microwave-design/awr-tx-line.html

[59] "High Reliability Glass Epoxy Multi-Layer Materials (High TG & Low CTE type)," Panasonic Holdings Corp., Kadoma, Japan. Accessed: Dec. 14, 2023. [Online]. Available: https://www.brandner.ee/wp-content/uploads/2017/08/DielectricConstants_R-1755V_R-1650V.pdf

[60] Brandner. "Impedance," Brandner.com. Accessed: Dec. 14, 2023. [Online]. Available: <https://www.brandner.ee/good-advice/impedance/>

[61] TDK Corporation, "Chip Antenna Simulation" product.tdk.com. Accessed: Dec. 14, 2023. [Online]. Available: <https://product.tdk.com/en/search/rf/rf/antenna/simulation>

[62] *Safety of transformers, reactors, power supply units and combinations thereof - Part 1: General requirements and tests*, EVS-EN IEC 61558-1:2019, MTÜ Eesti Standardimis- ja Akrediteerimiskeskus, Tallinn, Eesti, Jul. 2019. [Online]. Available: <https://www.evs.ee/et/evs-en-iec-61558-1-2019>

[63] *Audio/video, information and communication technology equipment - Part 1: Safety requirements*. EVS-EN IEC 62368-1:2020+A11:2020, MTÜ Eesti Standardimis- ja Akrediteerimiskeskus, Tallinn, Eesti, Apr. 2020. [Online]. Available: <https://www.evs.ee/en/evs-en-iec-62368-1-2020-a11-2020-consolidated>

[64] *Information technology equipment - Safety - Part 1: General requirements*, IEC 60950-1:2005, MTÜ Eesti Standardimis- ja Akrediteerimiskeskus, Tallinn, Eesti, Dec. 2005. [Online]. Available: <https://www.evs.ee/et/iec-60950-1-2005>

[65] "Energy saving high voltage converter for direct feedback." STMicroelectronics N.V, Geneva, Switzerland. Accessed: Mar. 16, 2023. [Online]. Available: <https://www.st.com/resource/en/datasheet/viper06.pdf>

[66] A. Cannone, "3 W, 5 V isolated flyback converter using the VIPer06HN, from the VIPerTM plus family," STMicroelectronics N.V, Geneva, Switzerland. Accessed: Mar. 16, 2023. [Online]. Available: https://www.st.com/resource/en/application_note/an4410-3-w-5-v-isolated-flyback-converter-using-the-viper06hn-from-the-viper-plus-family-stmicroelectronics.pdf

[67] "WE 750871013." we.online.com. Accessed: Dec. 20, 2023. [Online]. Available: <https://www.we-online.com/components/products/datasheet/750871013.pdf>

[68] "Offline Flyback Transformers." Accessed: Dec. 20, 2023. [Online]. Available: <https://www.we-online.com/en/components/products/MID-OLTI>

[69] "Application Note AN-4147 – Design Guidelines for RCD Snubber of Flyback Converters." e2e.ti.com. Texas Instruments Inc., Dallas, TX, USA. Accessed: Feb. 15, 2023. [Online]. Available: https://e2e.ti.com/cfs-file/__key/communityserver-discussions-components-files/196/Design-Guidelines-for-RCD-Snubber-of-Flyback-Converters_2D00_Fairchild-AN4147.pdf

[70] "15V/18W isolated SSR Flyback with VIPER318LDTR." STMicroelectronics N.V, Geneva, Switzerland. Accessed: Mar. 16, 2023. [Online]. Available: https://www.st.com/resource/en/application_note/an5558-15v18w-isolated-ssr-flyback-with-viper318ldtr-stmicroelectronics.pdf

[71] "ADP7142." analog.com. Accessed: Apr. 19, 2024. [Online]. Available: <https://www.analog.com/media/en/technical-documentation/data-sheets/adp7142.pdf>

Appendix 1 Power supply prototype schematic

